Since January 2020 Elsevier has created a COVID-19 resource centre with free information in English and Mandarin on the novel coronavirus COVID-19. The COVID-19 resource centre is hosted on Elsevier Connect, the company's public news and information website.

Cell Stem Cell

Article

Human Lung Stem Cell-Based Alveolospheres Provide Insights into SARS-CoV-2-Mediated Interferon Responses and Pneumocyte Dysfunction

Graphical Abstract

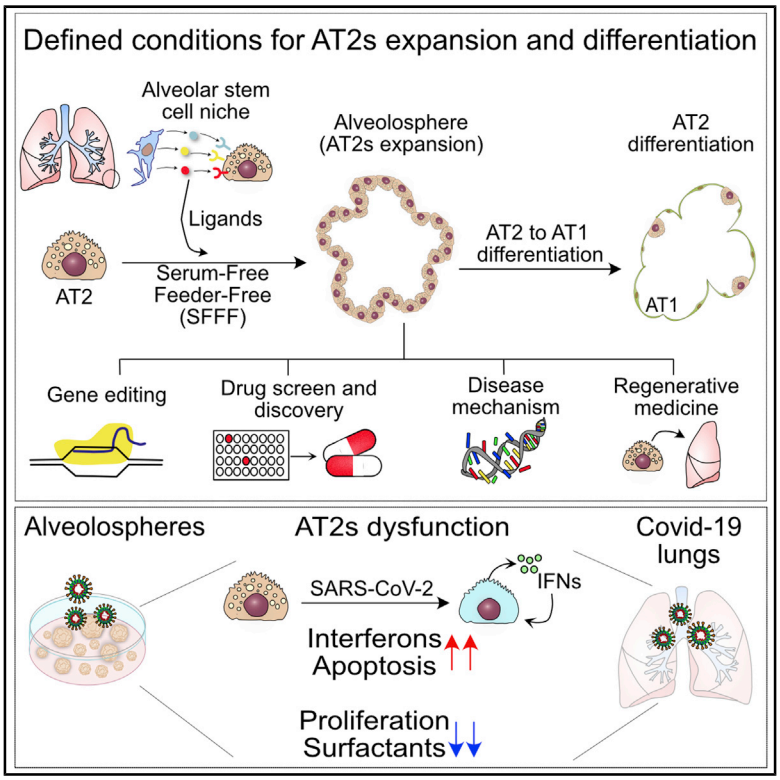

Highlights

- Stroma-free long-term expansion and differentiation of adult human lung stem cells
- AT2 response to SARS-CoV-2 infection mirrors features of COVID-19 lungs
- Infected AT2s upregulate IFNs and apoptotic pathways and decrease surfactants
- Low-dose IFN pre-treatment blocks SARS-CoV-2 replication in alveolospheres

Authors

Hiroaki Katsura, Vishwaraj Sontake, Aleksandra Tata, ..., Scott H. Randell, Ralph S. Baric, Purushothama Rao Tata

Correspondence

purushothamarao.tata@duke.edu

In Brief

Tata and colleagues report defined conditions for long-term expansion and differentiation of adult human primary alveolar stem cells. Cultured AT2s are conducive to SARS-CoV-2 infection and elicit transcriptome-wide changes that mirror COVID-19 histopathology, including upregulation of inflammatory responses, cell death, and downregulation of surfactant expression, leading to pneumocyte dysfunction.

Katsura et al., 2020, Cell Stem Cell *27*, 890–904
December 3, 2020
https://doi.org/10.1016/j.stem.2020.10.005

CellPress

CellPress

Cell Stem Cell

Article

Human Lung Stem Cell-Based Alveolospheres Provide Insights into SARS-CoV-2-Mediated Interferon Responses and Pneumocyte Dysfunction

Hiroaki Katsura,[1,11] Vishwaraj Sontake,[1,11] Aleksandra Tata,[1,11] Yoshihiko Kobayashi,[1,11] Caitlin E. Edwards,[2,11] Brook E. Heaton,[3] Arvind Konkimalla,[1,4] Takanori Asakura,[5] Yu Mikami,[5] Ethan J. Fritch,[6] Patty J. Lee,[7] Nicholas S. Heaton,[3] Richard C. Boucher,[5] Scott H. Randell,[8] Ralph S. Baric,[2,6] and Purushothama Rao Tata[1,9,10,12,*]

[1]Department of Cell Biology, Duke University School of Medicine, Durham, NC 27710, USA
[2]Department of Epidemiology, University of North Carolina at Chapel Hill, Chapel Hill, NC, USA
[3]Department of Molecular Genetics and Microbiology, Duke University School of Medicine, Durham, NC 27710, USA
[4]Medical Scientist Training Program, Duke University School of Medicine, Durham, NC 27710, USA
[5]Marsico Lung Institute, University of North Carolina at Chapel Hill, Chapel Hill, NC, USA
[6]Department of Microbiology and Immunology, University of North Carolina at Chapel Hill, Chapel Hill, NC, USA
[7]Division of Pulmonary, Allergy and Critical Care Medicine, Department of Medicine, Duke University Medical School, Durham, NC 27710, USA
[8]Department of Cell Biology and Physiology, The University of North Carolina at Chapel Hill, Chapel Hill, NC 27599, USA
[9]Duke Cancer Institute, Duke University School of Medicine, Durham, NC 27710, USA
[10]Regeneration Next, Duke University, Durham, NC 27710, USA
[11]These authors contributed equally
[12]Lead Contact
*Correspondence: purushothamarao.tata@duke.edu
https://doi.org/10.1016/j.stem.2020.10.005

SUMMARY

Coronavirus infection causes diffuse alveolar damage leading to acute respiratory distress syndrome. The absence of *ex vivo* models of human alveolar epithelium is hindering an understanding of coronavirus disease 2019 (COVID-19) pathogenesis. Here, we report a feeder-free, scalable, chemically defined, and modular alveolosphere culture system for the propagation and differentiation of human alveolar type 2 cells/pneumocytes derived from primary lung tissue. Cultured pneumocytes express the severe acute respiratory syndrome coronavirus 2 (SARS-CoV-2) receptor angiotensin-converting enzyme receptor type-2 (ACE2) and can be infected with virus. Transcriptome and histological analysis of infected alveolospheres mirror features of COVID-19 lungs, including emergence of interferon (IFN)-mediated inflammatory responses, loss of surfactant proteins, and apoptosis. Treatment of alveolospheres with IFNs recapitulates features of virus infection, including cell death. In contrast, alveolospheres pretreated with low-dose IFNs show a reduction in viral replication, suggesting the prophylactic effectiveness of IFNs against SARS-CoV-2. Human stem cell-based alveolospheres, thus, provide novel insights into COVID-19 pathogenesis and can serve as a model for understanding human respiratory diseases.

INTRODUCTION

In coronavirus disease 2019 (COVID-19), lung disease is the primary cause for mortality. Histopathological analyses reveal widespread alveolar damage and pneumonia, which may eventually progress to acute respiratory distress syndrome (ARDS) (Bradley et al., 2020). This clinically challenging manifestation is accompanied by the production of multiple cytokines (“cytokine storm”), loss of parenchyma, immune infiltration, and fluid filled alveoli, all of which contribute to acute respiratory failure and eventual death (Huang et al., 2020a; Zhu et al., 2020). The causative agent of COVID-19 is the novel coronavirus severe acute respiratory syndrome coronavirus 2 (SARS-CoV-2). This virus uses the same receptor—ACE2 (angiotensin-converting enzyme receptor type-2)—for entry into target cells as the closely related viruses SARS-CoV (2003) and NL-63 (Hoffmann et al., 2020). However, the unique clinical symptoms and increased transmissibility of SARS-CoV-2 suggest that it uses different mechanisms to both infect and evade host immune responses, including the production of type I and type III interferons (IFN-IIIs) (Hou et al., 2020; Huang et al., 2020a; Wu and McGoogan, 2020; Zhu et al., 2020). To develop safe and effective therapies for COVID-19, it is critically important to understand the cell-type-specific innate immune mechanisms triggered in response to viral entry and how they orchestrate adaptive immune responses. One way to achieve this goal is to

infect target cells of the adult human lung with virus *ex vivo* and to follow molecular and cellular responses over time. Ideally, this approach must be performed under well-defined, modular conditions that can easily be adapted to high-throughput pharmacogenomic screens for therapeutic discovery. We report here the results of this approach by using SARS-CoV-2 infection of 3D alveolosphere cultures of primary human alveolar epithelial type-2 cells (AT2s), the stem cells of the distal alveolar region.

Single-cell transcriptome profiling and immunolocalization studies showed that AT2s exhibit the highest enrichment of SARS-CoV-2 receptor ACE2, and its associated protease TMPRSS2, in the human distal lung (Hou et al., 2020; Muus et al., 2020; Sungnak et al., 2020; Ziegler et al., 2020). AT2s can both self-renew and differentiate into thin and flat gas exchanging alveolar epithelial type-1 cells (AT1s). In addition, they secrete surfactant proteins, namely, SFTPA and SFTPD, that promote alveolar patency but also can directly bind many viruses and other microbial pathogens to facilitate opsonization and phagocytosis (Crouch and Wright, 2001; McCormack and Whitsett, 2002). Therefore, AT2s play a key role in providing a first line of defense against viruses and in restoring cell numbers after injury. However, currently we do not know the nature of the pathways that are dysregulated in human AT2s in response to SARS-CoV-2 infection and how these pathways intersect with other forms of defense mechanisms. It is also unclear whether and how AT2s maintain stem cell characteristics while activating anti-viral defense mechanisms. Alveolosphere cultures derived from adult AT2s provide the opportunity to address these questions.

Numerous studies have demonstrated the potential of primary-tissue-derived organoids to serve as models for disease pathogenesis, organogenesis, and tissue repair (Drost and Clevers, 2018; Jacob et al., 2017; Lancaster and Huch, 2019; Lancaster and Knoblich, 2014; Neal et al., 2018; Yamamoto et al., 2017). For example, recent studies using intestinal organoids combined with SARS-CoV-2 infection revealed the infectability of intestinal epithelium and associated cellular responses (Lamers et al., 2020; Yang et al., 2020). In the case of the lung, AT2s have the ability to generate alveolospheres, which can proliferate and differentiate into AT1s (Barkauskas et al., 2013, 2017; Chung et al., 2018; Dye et al., 2015; Hogan and Tata, 2019; Katsura et al., 2019; Lancaster and Knoblich, 2014; Lee et al., 2013; Nikolić et al., 2018; Shiraishi et al., 2019a). However, current conditions require the co-culture of AT2s with PDGFRα^+ fibroblasts isolated from the alveolar stem cell niche or lung endothelial cells isolated from fetal tissues (Barkauskas et al., 2017; Lancaster and Huch, 2019; McQualter et al., 2010). In addition, current culture media are poorly defined and contain unknown factors derived from fetal bovine serum (FBS) or calf serum and bovine pituitary extracts (Barkauskas et al., 2017). Such complex conditions do not provide a modular system in which AT2s can be either selectively expanded or differentiated into AT1 (Shiraishi et al., 2019a, 2019b; Weiner et al., 2019). Such defined conditions are needed to study cell-type-specific effects and for high-throughput pharmaco-genomic studies to discover drugs for treating diseases.

To overcome these challenges, we have developed chemically defined conditions for human AT2 expansion and differentiation in alveolosphere cultures. We demonstrate that SARS-CoV-2 infects and propagates in AT2s in these alveolospheres. Complementary assays were used to assess the transcriptome-wide changes in response to SARS-CoV-2 infection, and the results were directly compared with transcriptome data from COVID-19 patients. Furthermore, we show that viral infection induces the production of IFNs and that different types of IFNs affect AT2 behavior in alveolosphere culture.

RESULTS

Establishment of Chemically Defined Conditions for Alveolosphere Cultures

The cellular composition and properties of 3D culture models are highly dependent on culture conditions (Barkauskas et al., 2017; Drost and Clevers, 2018; Hu et al., 2018; Huch et al., 2013; Neal et al., 2018; Peng et al., 2018; Velasco et al., 2019). Purified, lineage-labeled mouse AT2s can be grown as alveolospheres (Barkauskas et al., 2013, 2017; Katsura et al., 2019; Lee et al., 2013). However, current culture conditions use a complex medium containing many variable components (serum and bovine pituitary extract) and require the addition of lung-resident PDGFRα^+ fibroblasts to support AT2 growth. We, therefore, established defined conditions for long-term propagation of AT2s. Initially we used mouse cells, and then subsequently similar conditions were adapted for human AT2 cultures. Briefly, we performed single-cell transcriptome analysis on AT2s grown in mouse tracheal epithelial cell (MTEC) media (Figures S1A and S1B) and then mined the single-cell RNA sequencing (scRNA-seq) data for ligand-receptor pairs differentially expressed in epithelial cells and fibroblasts (Figures S1C and S1D). Based on these data, we tested different combinations of ligands and small molecules, including interleukin-1β (IL-1β), a recently identified AT2 niche-derived molecule, in a basal medium to generate a serum-free feeder-free medium (SFFF) (Figures S1E–S1H; see Table S1 for the full composition of the medium) (Katsura et al., 2019). SFFF medium supports the growth of AT2s characterized by numerous mature lamellar bodies packed with surfactants (Figure S1I). Of note, although the addition of IL-1β enhanced alveolosphere size, it did not increase alveolosphere number. Recent studies identified that inhibition of bone morphogenetic protein (BMP) signaling prevents AT2 differentiation (Chung et al., 2018). Therefore, to promote a higher proportion of AT2s in alveolospheres, we supplemented SFFF medium with inhibitors of BMP signaling (Noggin and DMH1), to generate AT2 maintenance medium (AMM) (Figure S2A). In this medium, pneumocytes maintain AT2 identity and can be sub-cultured for over six passages (Figures S2B–S2F). Furthermore, we formulated a medium (AT2 differentiation medium [ADM]) that contains 10% FBS and stimulated AT2 differentiation, leading to a dramatic induction of cells expressing markers of AT1s (see Table S1 for the full composition of the media; Figures S2G and S2H).

Defined Culture Conditions for Human Alveolosphere Cultures

Next, we sought to establish SFFF culture conditions for human AT2s. We purified AT2s from healthy lungs using HTII-280 antibody (Gonzalez et al., 2010) and established alveolosphere cultures using SFFF medium with human-specific recombinant proteins in the absence of stromal cells (Table S2; Figure S3A).

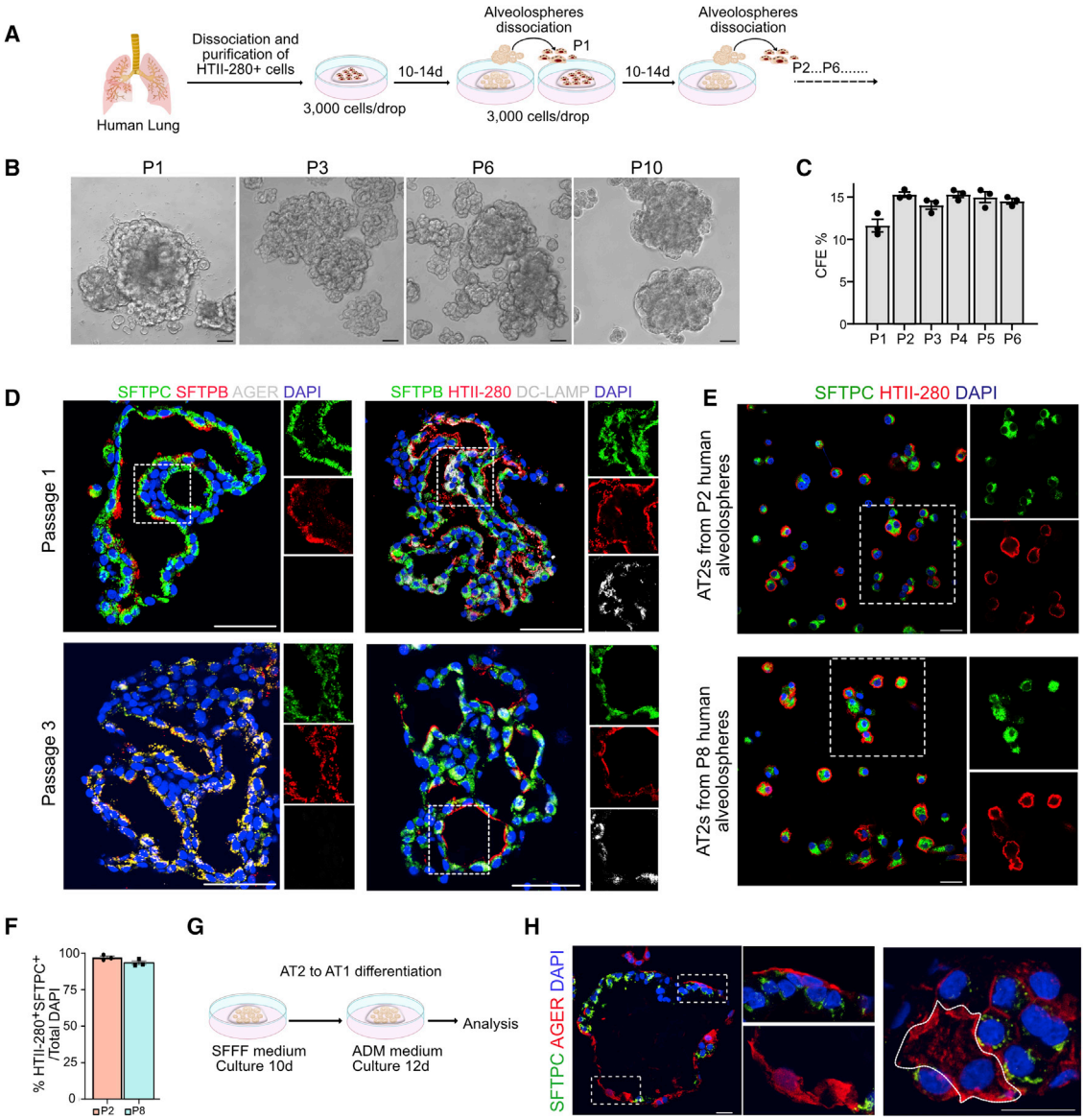

Figure 1. Establishment of Chemically Defined Human Lung Alveolosphere Culture System

(A) Schematic representation of human alveolosphere cultures and passaging in SFFF medium.

(B) Representative images of human alveolospheres from different passages. Scale bar: 100 μm.

(C) Quantification of the colony formation efficiency (CFE) of human alveolospheres at different passages.

(D) Immunostaining for SFTPC (green), SFTPB (red), and AGER (gray) (left panel) or SFTPB (green), HTII-280 (red), and DC-LAMP (gray) (right panel) at P1 and P3 human alveolospheres cultured in SFFF medium for 14 days.

(E) Immunostaining for SFTPC (green) and HTII-280 (red) in cells dissociated from alveolospheres at P2 (top) and P8 (bottom).

(F) Quantification of HTII-280$^+$ SFTPC$^+$ cells/total 4′,6-diamidino-2-phenylindole (DAPI)$^+$ cells derived from alveolospheres dissociation from P2 (orange) and P8 (blue).

(G) Schematic representation of human AT2 to AT1 differentiation in alveolospheres. AT2s were cultured in SFFF medium for 10 days, followed by culture in ADM for 14 days.

(H) Immunostaining for SFTPC (green) and AGER (red) in human alveolospheres cultured under ADM condition for 14 days. Scale bars: 100 μm (B); 50 μm (D); 20 μm (E); 20 μm (H). DAPI (blue) shows nuclei in (D), (E), and (H). Data are presented as mean ± SEM.

Anddition of IL-1β for the first 4–7 days of culture slightly enhanced the size and number of alveolospheres, although this effect varied in magnitude from donor to donor (Figures S3B–S3D). Therefore, we did not use IL-1β treatment for further experiments. Long-term sub-culture over 10 passages and sphere quantification (P6) confirmed the ability of SFFF medium to sustain long-term human AT2 self-renewal and maintenance of morphology across passages (Figures 1A–1C; Figures S3E and S3F). Immunostaining for general lung epithelial cell (NKX2-1) and AT2-specific markers (SFTPC, SFTPB, HTII-280,

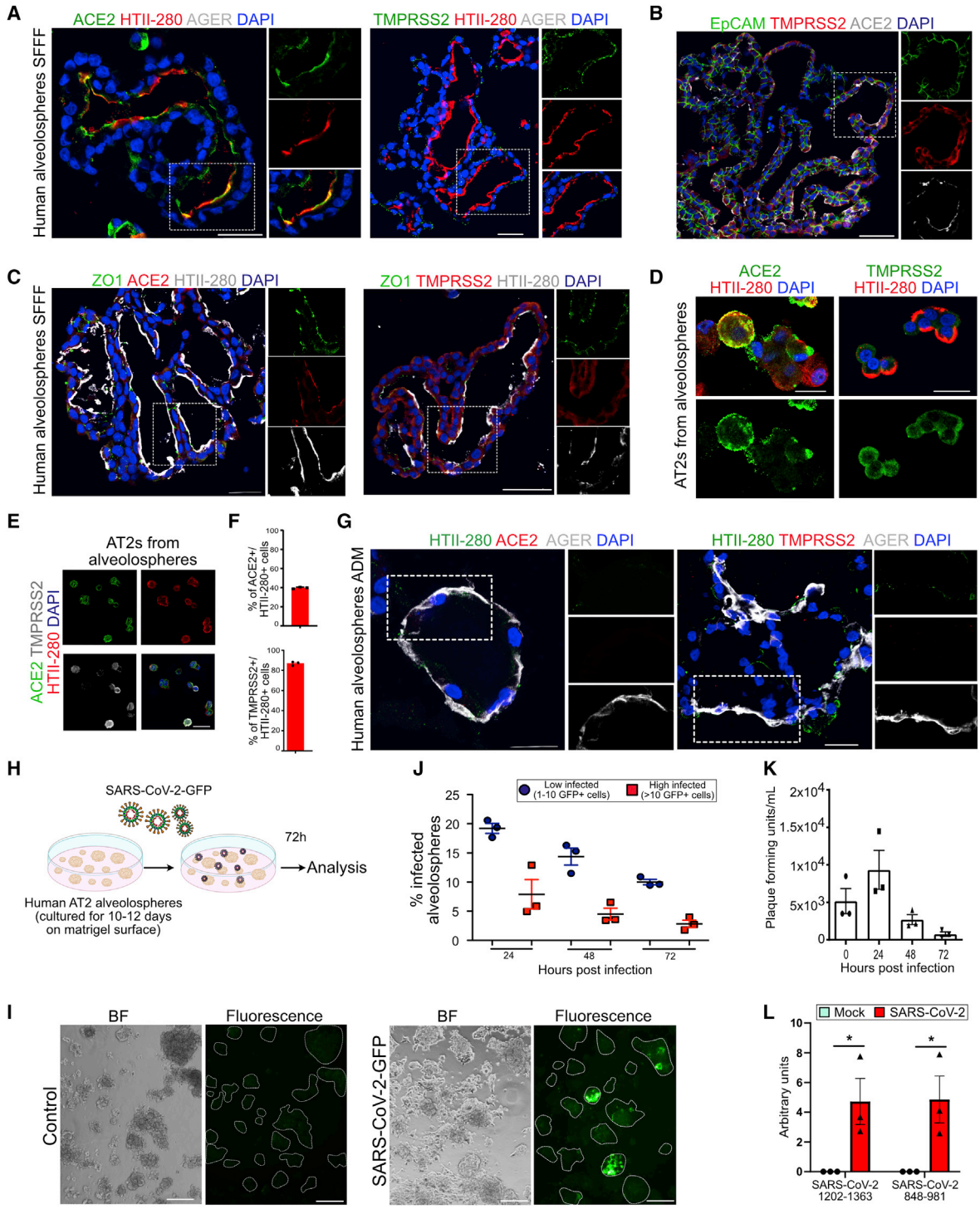

Figure 2. Alveolosphere-Derived AT2s Express Viral Receptors and Are Permissive to SARS-CoV-2 Infection

(A) Immunostaining for ACE2 (green) (left panel) and TMPRSS2 (green) (right panel) with HTII-280 (red) and AGER (gray).

(B) Co-staining for epithelial cell membrane marker EPCAM (green) with TMPRSS2 (red) and ACE2 (gray).

(C) Co-staining for ACE2 (red) (left panel) and TMPRSS2 (red) (right panel) with polarity marker ZO1 (green) and HTII-280 (gray).

(D) Co-immunostaining for ACE2 (green) (left panel) and TMPRSS2 (green) (right panel) with HTII-280 (red) in AT2s dissociated from P5-cultured alveolospheres.

(E) Co-immunostaining for ACE2 (green), HTII-280 (red), and TMPRSS2 (gray) in AT2s from alveolospheres.

(F) Quantification of percent ACE2^{+}/total HTII-280^{+} cells (left) and percent TMPRSS2^{+}/total HTII-280^{+} cells.

(G) Immunostaining for ACE2 (red) (left panel) and TMPRSS2 (red) (left panel) with HTII-280 (green) and AGER (gray) in alveolospheres cultured in ADM for 14 days.

(legend continued on next page)

and DC-LAMP) revealed that alveolospheres were composed solely of AT2s and that neither airway (SOX2, SCGB1A1, and TP63) nor AT1s (AGER) were present (Figures 1D–1F; Figures S3G and S3H). Quantitative RT-PCR (qRT-PCR) analyses for AT2 markers further corroborated these findings (Figure S3F).

To induce the differentiation of AT2s, we first tested differentiation medium containing 10% bovine serum, but there were few or no AGER$^+$ (AT1) cells in alveolospheres (Figure S3I). We therefore switched to human serum and found that this change induced a robust expression of the AT1 marker AGER that was co-incident with a decrease in SFTPC (Figures 1G and 1H; Figure S3J). Significantly, the AGER$^+$ cells show the large, thin, and flat morphology characteristic of type-1 pneumocytes *in vivo* (Figure 1H). Collectively, these data indicate that our newly developed SFFF culture conditions facilitated the long-term expansion of primary human AT2s in the absence of feeder cells and that the addition of human serum stimulated the cells to differentiate into AT1s.

Alveolosphere-Derived AT2s Express Viral Receptors and Are Permissive to SARS-CoV-2 Infection

Recent studies have indicated that SARS-CoV-2 receptor ACE2 and a key protease, TMPRSS2, which is needed for proteolytic cleavage of the viral spike protein, are expressed in AT2s (Hoffmann et al., 2020; Hou et al., 2020; Muus et al., 2020; Sungnak et al., 2020; Ziegler et al., 2020). We therefore assessed the expression and localization of ACE2 and TMPRSS2 in pneumocytes derived from alveolospheres cultured in SFFF media or ADM that contain AT2s only or a mixture of AT2 and AT1s, respectively. Immunostaining in combination with a well-known apical marker of AT2 (HTII-280), polarity marker ZO1, and membrane marker EpCAM showed that ACE2 is localized at the apical surface (similar to HTII-280 and ZO1), whereas TMPRSS2 is enriched at the basal side of AT2s (Figures 2A–2C). We then quantified the number of AT2s that express ACE2 and TMPRSS2 on single-cell preparations of alveolospheres. Our data revealed that 40% of AT2s express ACE2, whereas about 80% are positive for TMPRSS2 (Figures 2D–2F). We did not find ACE2 and TMPRSS expression in differentiated (AGER$^+$) AT1s, a finding consistent with prior single-cell transcriptome as well as immunolabeling assays on human lungs (Figure 2G; Hou et al., 2020; Muus et al., 2020).

To test whether SARS-CoV-2 can infect alveolosphere-derived AT2s, we used a recently developed reverse-engineered SARS-CoV-2 virus harboring a GFP-fusion protein (Hou et al., 2020). Human alveolospheres were cultured on a Matrigel surface in SFFF media (lacking IL-1β) for 10–12 days, incubated with SARS-CoV-2-GFP for 2 h, washed with phosphate-buffered saline (PBS) to remove residual viral particles, and then collected for analysis over 72 h. GFP was detected as early as 48 hours post-infection (hpi) in virus-exposed but not in control alveolospheres (Figures 2H and 2I). Quantification of GFP-expressing cells at 24, 48, and 72 hpi revealed a gradual decrease in the number of GFP+ cells (Figure 2J). Consistent with this finding, plaque-forming assays using culture supernatants revealed that viral release peaks at 24 h but later declined (Figure 2K). This observation was consistent across cells from three different donors. Of note, we observed a significant number of viral particles immediately after infection despite numerous washes with PBS. This result was likely due to the entrapment of virus in the Matrigel. Nevertheless, the viral titer increased at 24 hpi, demonstrating that SARS-CoV-2 productively replicates in AT2s (Figure 2K). qRT-PCR further revealed the presence of viral RNA in SARS-CoV-2-infected cells compared to controls (Figure S4A). To further confirm virus replication, we performed qRT-PCR using primers that specifically recognize the minus strand of the virus. Indeed, we observed viral replication in alveolosphere cultures (Figure 2L).

AT2s Activate IFN and Inflammatory Pathways in Response to SARS-CoV-2 Infection

To gain insights into the response of AT2s to SARS-CoV-2 (wild type), we performed unbiased genome-wide transcriptome profiling on alveolospheres cultures 48 h after infection (Figure 3A). Of all the sequenced reads, viral transcripts accounted for 4.7%, indicating that virus was propagating in AT2s (Figure S4B). Previous studies have shown that in response to viral infection, target cells typically produce type I IFNs (IFN-Is) and IFN-IIIs (α/β and λ, respectively) that subsequently activate targets of transcription factors IRF, STAT1/2, and NF-κB including, IFN-stimulated genes (ISGs), inflammatory chemokines, and cytokines that go on to exert anti-viral defense mechanisms (Barrat et al., 2019). It was therefore significant that a differential gene expression analysis of infected versus uninfected alveolospheres revealed an enrichment of transcripts related to general viral response genes, including multiple IFNs and their targets (Figures 3A–3F). Specifically, SARS-CoV-2-infected AT2s were enriched for transcripts of IFN-Is (*IFNA7*, *IFNB1*, and *IFNE*) as well as IFN-IIIs (*IFNL1*, *IFNL2*, and *IFNL3*) but not type II IFN (IFNG) ligands (Figures 3B and 3C; Figure S4C). Receptors for IFN-Is (*IFNAR1* and *IFNAR2*), type II IFNs (*IFNGR1 and IFNGR2)* and IFN-IIIs (*IFNLR1* and *IL10RB*) were expressed in control AT2s, and a modest increase was found for *IFNAR2* and *IFNGR2* after SARS-CoV-2 infection (Figures 3B and 3D; Platanias, 2005; Syedbasha and Egli, 2017). These data indicate that in response to SARS-CoV-2 infection, AT2s produce IFN-I and IFN-III ligands, which can potentially act by either by autocrine or paracrine (neighboring AT2s) mechanisms to activate their cognate

(H) Schematic representation for SARS-CoV-2-GFP infection in human alveolospheres. AT2s were cultured on Matrigel-coated plates in SFFF medium for 10–12 days, followed by infection with SARS-CoV-2 virus and RNA isolation or histological analysis after different time points.

(I) Representative wide-field microscopy images from control and SARS-CoV-2-GFP-infected human lung alveolospheres.

(J) Quantification of low-infected (1–10 GFP$^+$ cells) and high-infected (10 or more GFP$^+$ cells) alveolospheres 24, 48, and 72 h post SARS-CoV-2GFP virus infection.

(K) Viral titers were measured by plaque assays using media collected from lung alveolosphere cultures at 24, 48, and 72 h post-infection.

(L) SARS-CoV-2 negative-strand-specific reverse transcription followed by qRT-PCR targeting two different genomic loci (1202–1363 and 848–981) in mock- (blue) and SARS-CoV-2-infected human alveolospheres at 72 h post-infection. Asterisks show $p < 0.05$. Scale bars: 30 μm (A, B, and C); 20 μm (D); and 20 μm (F). White box in merged image indicates region of single-channel images. All quantification data are presented as mean ± SEM.

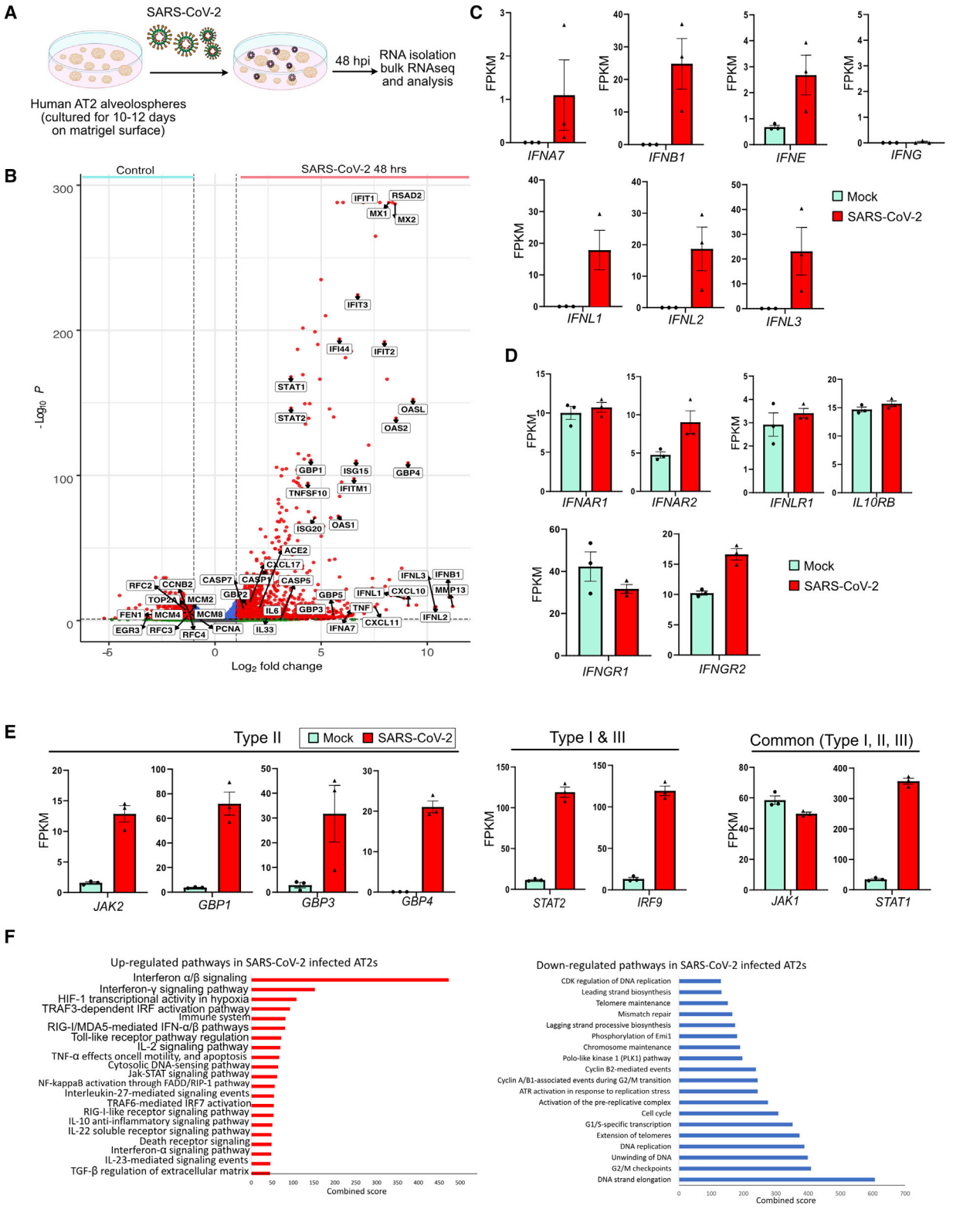

Figure 3. Transcriptome Profiling Revealed Enrichment of IFN, Inflammatory, and Cell Death Pathways in SARS-CoV-2-Infected Pneumocytes

(A) Schematic for SARS-CoV-2-GFP infection in human alveolospheres. AT2s cultured in SFFF medium were infected with SARS-CoV-2 virus followed by RNA isolation at 48 h after infection.

(legend continued on next page)

receptors. Indeed, a large number of IFN target genes including ISGs, IFN-induced protein-coding genes (IFIs), and IFN-induced protein with tetratricopeptide repeats-coding genes (IFITs), were upregulated in SARS-CoV-2-infected AT2s (Figures 3B and 3E). Additionally, key transcription factors STAT1 and STAT2 that are known to be components of the signaling pathways downstream of IFN receptors were also upregulated in infected AT2s.

Pathway analysis revealed all three classes of IFN targets were upregulated, but the most prominent were IFN-I and IFN-III signaling. Despite the absence of type II IFN ligands (*IFNG*), we observed a significant upregulation of canonical targets of IFNγ-response mediators in SARS-CoV-2-infected AT2s (Figures 3B and 3E). This finding suggests that there is a significant overlap of downstream targets and cross-talk between different classes of IFN pathways, as described previously (Barrat et al., 2019; Bartee et al., 2008). Other prominent upregulated genes include chemokines (*CXCL10*, *CXCL11*, and *CXCL17*) and programmed cell-death-related genes (*TNFSF10*, *CASP1*, *CASP4*, *CASP5*, and *CASP7*) (Figure 3B; Figures S4D and S4E). In contrast, we observed a significant downregulation of transcripts associated with DNA replication and cell cycle (*PCNA*, *TOP2A*, *MCM2*, and *CCNB2)* in infected AT2s (Figure 3B; Figure S4F). Selected targets were validated using independent qRT-PCR assays at early (48 h) and late (120 h) time points post-infection (Figure S5A). Taken together, transcriptome analysis revealed a significant upregulation of IFN and inflammatory and cell death signaling, juxtaposed to the downregulation of proliferation-related transcripts, in alveolosphere-derived AT2s in response to SARS-CoV-2.

SARS-CoV-2 Infection Induces Loss of Surfactants and Pneumocyte Death

To gain further insights into how primary AT2s respond early to SARS-CoV-2 infection, we analyzed cellular changes in alveolospheres by using immunohistochemistry (Figure 4A). Quantification of infected alveolospheres revealed that 29.22% are $SARS^+$ (Figure 4B). Immunostaining revealed the co-expression of GFP and SARS-CoV-2 spike protein in infected alveolospheres (Figure 4C). We found variation in the number of GFP^+ cells in each alveolosphere. Therefore, we broadly categorized alveolospheres into low (1–10 cells) and high (>10) groups, depending on the number of $SARS^+$ cells in each alveolosphere (Figures 4C and 4D). Next, analyses for AT2 markers, including SFTPC, SFTPB, and HTII-280, revealed a dramatic loss or decrease in the expression of surfactant proteins SFTPC and SFTPB in infected cells (GFP^+ or $SARS^+$) but not in control alveolospheres (Figures 4C and 4E; Figure S5B). Of note, HTII-280 expression was unchanged (Figure S5C). The loss of surfactant protein expression was more apparent in highly infected alveolospheres (Figure S5B). Some of the GFP^+ cells showed a slightly elongated morphology, resembling that of AT1s, but immunostaining for AT1 markers revealed that infected cells did not differentiate into AT1s (Figure S5D). These data are in accordance with our scRNA-seq data that AT2s downregulate surfactant expression in response to SARS-CoV-2 infection.

Histopathological evidence suggests that there is a loss of alveolar parenchyma in COVID-19 lungs (Bradley et al., 2020; Huang et al., 2020a). To test whether SARS-CoV-2 infection induces cell death, we performed immunostaining for active caspase-3, a marker for apoptotic cells. Apoptotic cells were found in alveolospheres exposed to virus but not in controls, suggesting that AT2s undergo cell death in response to SARS-CoV-2 infection (Figure 4F). Significantly, we observed cell death in both $SARS^+$ and $SARS^-$ cells suggesting a paracrine mechanism inducing cell death in uninfected neighboring cells (Figure 4G). Furthermore, immunostaining for Ki67, a marker for proliferating cells revealed no apparent difference in overall cell replication in virus-exposed alveolospheres compared to controls (Figure 4H). Taken together, these data show that SARS-CoV-2 infection induces the downregulation of surfactant proteins and an increase in cell death in AT2s by both cell autonomous and non-autonomous mechanisms.

Transcriptome-wide Similarities in AT2s from SARS-CoV-2-Infected Alveolospheres and COVID-19 Lungs

To directly compare SARS-CoV-2-induced responses in AT2s in alveolospheres to changes seen in COVID-19 lungs, we used a publicly available scRNA-seq dataset from bronchoalveolar lavage fluid (BALF) obtained from six severe COVID-19 patients (Bost et al., 2020; Liao et al., 2020). First, we compared the gene expression profiles of AT2s from COVID-19 patient lungs with AT2s from healthy lungs (Figures S6A–S6D). We found a significant upregulation of chemokines (*CXCL10*, *CXCL14*, and *IL32)*, IFN targets (*IFIT1*, *ISG15*, and *IFI6*), and cell-death-pathway (*TNFSF10*, *ANXA5*, and *CASP4*) -related transcripts in COVID-19 patient AT2s (Figures 5A and 5B). Intriguingly, surfactant genes, including *SFTPA1*, *SFTPA2*, *SFTPB*, *SFTPC*, and *SFTPD*, as well as *NAPSA*, a gene product that catalyzes the processing of the pro-form of surfactant proteins into mature proteins, were significantly downregulated in COVID-19 patient AT2s, whereas changes in other AT2 markers were minimal and insignificant (Figures 5A and 5B). Pathway analysis revealed a significant enrichment for IFN-I and type II IFN signaling, inflammatory programs, and cell death pathways in COVID-19 AT2s (Figures 5C and 5D). We then made a direct comparison of transcripts between AT2s from SARS-CoV-2-infected *ex vivo* cultures and COVID-19 patient lungs. This comparison revealed a striking similarity in upregulated transcripts (Figure S6E). These included an upregulation of chemokines and cytokines, including IFN ligands and their targets, indicating that AT2s derived from alveolospheres respond similarly to AT2s from human lungs after SARS-CoV-2 infection (Figures S6E and S6F). We then extended these findings to COVID-19 lungs and uncovered that *SFTPB* but not other AT2s markers, NKX2-1 or ABCA3, were downregulated

(B) Volcano plot showing upregulated (right) and downregulated (left) genes in alveolospheres cultured in SFFF infected with SARS-CoV-2. DESeq2 was used to perform statistical analysis.

(C–E) Expression levels of listed genes in mock- (green) and SARS-CoV-2-infected (red) human alveolospheres detected by bulk RNA-seq. IFN ligands (C), receptors (D), as well as downstream targets (E), are shown. Data are presented as fragments per kilobase million (FPKM) mean ± SEM.

(F) Pathway enrichment analysis of upregulated (left, red) and downregulated (right, blue) genes in SARS-CoV-2-infected alveolospheres. Scale shows the combined score obtained from BioPlanet database through Enrichr.

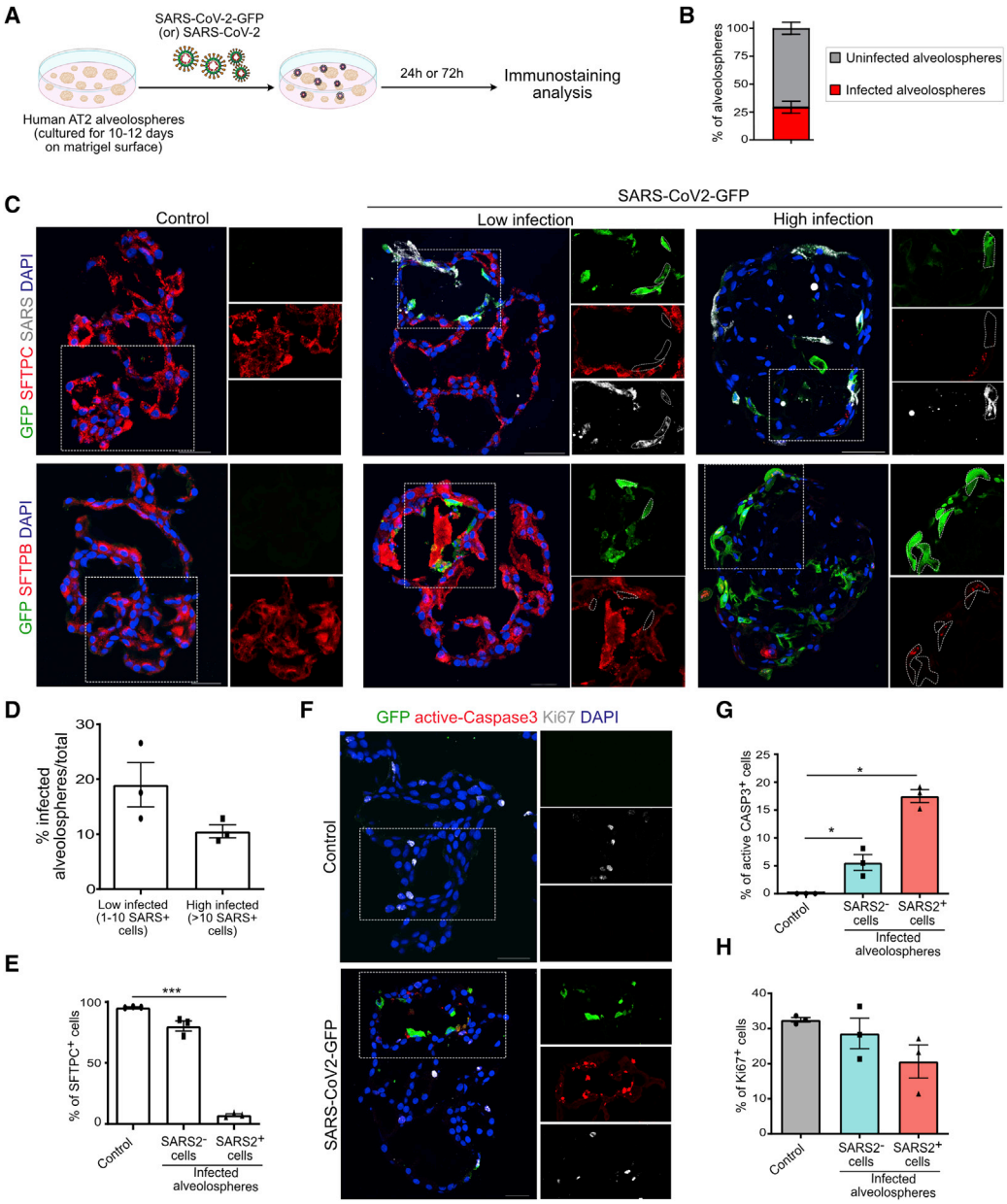

Figure 4. SARS-CoV-2 Infection Induces Loss of Surfactants and AT2 Death

(A) Schematic for SARS-CoV-2-GFP infection in human alveolospheres. Alveolospheres were cultured in SFFF medium, infected with SARS-CoV-2 virus, and collected for histological analysis.

(B) Quantification of the percentage of SARS-CoV-2-infected alveolospheres.

(C) Immunostaining for GFP (green), SFTPC (red), and SARS (gray) (top panel) and GFP (green) and SFTPB (red) (bottom panel) in control, "low," and "high" SARS-CoV-2-GFP-infected human lung alveolospheres at 72 h post-infection. Scale bar: 50 μm.

(D) Quantification of low-infected (1–10 SARS-CoV-2$^+$ cells) and high-infected (10 or more SARS-CoV-2$^+$ cells) alveolospheres.

(E) Quantification of SFTPC$^+$ cells in uninfected control and SARS$^-$ and SARS$^+$ cells in virus-infected alveolospheres.

(F) Immunostaining for GFP (green) in combination with the apoptotic marker active caspase 3 (red) and proliferation marker Ki67 (gray) in control and SARS-CoV-2-GFP-infected alveolospheres. Scale bar: 30 μm.

(G and H) Quantification of active caspase-3 (CASP3)$^+$ (G) and Ki67$^+$ (H) cells in uninfected control (gray), SARS-CoV-2$^-$ cells (blue), and SARS-CoV-2$^+$ cells in infected alveolospheres. The white box in the merged image indicates the region of single-channel images. DAPI stains nuclei (blue). All quantification data are presented as mean ± SEM.

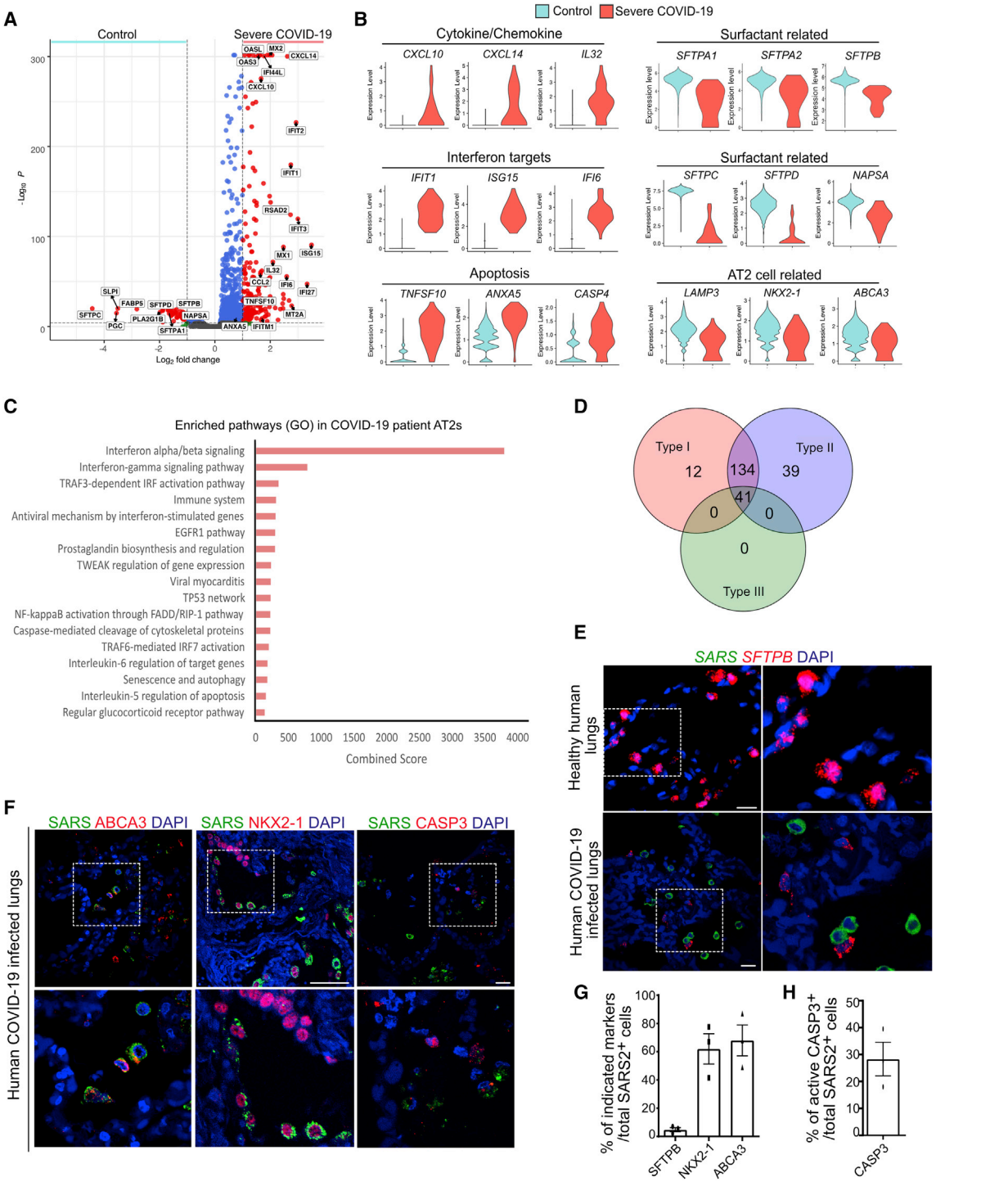

Figure 5. Transcriptome-wide Similarities in AT2s from SARS-CoV-2-Infected Alveolospheres and COVID-19 Lungs

(A) Volcano plot shows specific genes enriched in AT2s in bronchioalveolar lavage fluid from severe COVID-19 patients (right) and AT2s isolated from healthy lungs (control) (left). Wilcoxon rank-sum test was used for the statistical analysis.

(B) Violin plots show gene expression of cytokines and chemokines (*CXCL10*, *CXCL14*, and *IL32*), interferon targets (*IFIT1*, *ISG15*, and *IFI6*), apoptosis targets (*TNFSF10*, *ANXA5*, and *CASP4*), surfactant-related targets (*SFTPC*, *SFTPD*, and *NAPSA*), and AT2-related targets (*LAMP3*, *NKX2-1*, and *ABCA3*) in AT2s derived from control and severe COVID-19 patient lungs.

(C) Pathway enrichment analysis shows signaling pathways enriched in AT2s derived from severe COVID-19 patients. Scale shows combined score obtained from BioPlanet database through Enrichr.

(legend continued on next page)

in SARS$^+$ cells (Figures 5E–5G). Similar to alveolospheres, we observed active caspase-3 in SARS$^+$ cells in COVID-19 human lungs (Figure 5H).

AT2s Respond to Exogenous IFNs and Recapitulate Features Associated with SARS-CoV-2 Infection

Our transcriptome analysis revealed a striking similarity in IFN signatures in AT2s from alveolospheres and human lungs after SARS-CoV-2 infection. Previous studies have shown that IFNs induce cellular changes in a context-dependent manner. For example, IFNα and IFNβ provide protective effects in response to influenza virus infection in the lungs, whereas IFNγ induces apoptosis in intestinal cells in response to chronic inflammation (Koerner et al., 2007; Takashima et al., 2019). To test the direct effects of IFNs on AT2s, we treated alveolospheres with purified recombinant IFNα, IFNβ, and IFNγ in SFFF media and cultured them for 72 h (Figure 6A). First, we observed detached cells in all treatments, with a maximal ~3-fold increased effect in IFNγ-treated alveolospheres (Figure 6B). Immunostaining for active caspase-3 revealed a significant induction of cell death in response to all IFN treatments, with a maximal effect with IFNγ (Figures 6C and 6D; Figure S7A). In contrast, we observed a significant reduction in cell proliferation in IFNβ and IFNγ treatments, as revealed by immunostaining for Ki67, a marker for cell proliferation (Figures 6E and 6F). Significantly, immunostaining revealed a reduction of SFTPB expression in alveolospheres treated with all IFNs compared with that of controls (Figure 6E). A similar trend was observed for *SFTPC* and *SFTPB* transcripts, as assessed by qRT-PCR (Figures S7B and S7C). These data are in accordance with transcriptome data from AT2 alveolospheres after SARS-CoV-2 infection (Figure 3B). Of note, treatment with IFNα, IFNβ, and IFNγ significantly enhanced the levels of *ACE2*, but not *TMPRSS2* transcripts, which is in line with results of previous studies in other cell types (Hou et al., 2020; Ziegler et al., 2020; Figures S7D and S7E). A similar trend was observed in SARS-CoV-2-infected cells, suggesting a positive loop that involves IFNs and ACE2 that subsequently amplifies SARS-CoV-2 infection (Figure S7F).

Pre-treatment with IFNs Reduces SARS-CoV-2 Replication in Alveolospheres

Recent studies suggested that pre-treatment with IFNs reduced SARS-CoV-2 replication in Calu-3 and Vero-2 cells. We then tested the effect of pre-treatment of alveolospheres with IFNs before viral infection (Clementi et al., 2020; Felgenhauer et al., 2020) because our above data from IFN treatments alone led to an increase in AT2 death. Therefore, we pre-treated alveolospheres with a lower dose of IFNα and IFNγ (10 ng) for 18 h prior to viral infection (Figure 6G). Subsequent plaque-forming assays at 24 hpi and 48 hpi revealed that pre-treatment with IFNs significantly reduced the viral titers in alveolospheres (Figure 6H). In addition, we also tested the effect of IFN signaling inhibition on viral replication. For this test, we pretreated alveolospheres with ruxolitinib, an inhibitor of IFN signaling, for 18 h and continued treatment following viral infection (Figure 6G). Plaque-forming assays revealed an increase in the viral replication (Figure 6H). Taken together, these data suggest that pre-treatment with IFNs gives a prophylactic effect, whereas IFN inhibition promotes viral replication.

DISCUSSION

Here, we used scRNA-seq-guided AT2-fibroblast interactome maps to develop and optimize the first chemically defined, serum-free, and stroma-free alveolosphere culture conditions for mouse and human AT2 expansion, maintenance, and differentiation. Our newly developed alveolosphere conditions facilitate long-term passaging and large-scale expansion, features conducive to infection by viruses and potentially other pathogens, as well as large-scale biochemical assays. Furthermore, our alveolosphere culture conditions are well suited for high-throughput, pharmaco-genomic screening to identify both antiviral drugs and pathways that control cell fate choices in certain pathophysiological conditions.

Using alveolosphere cultures, we demonstrate that AT2s express a SARS-CoV-2 receptor, ACE2, and are sensitive to virus infection. Transcriptome profiling further revealed the emergence of an ''inflammatory state'' in which AT2s activated the expression of numerous IFNs, cytokines, chemokines, and cell-death-related genes at later times post-infection. These data are consistent with earlier studies showing delayed host innate immune responses after SARS-CoV (2003) infection, until later times (Menachery et al., 2014), but also underscore the need for kinetic analyses of host responses at different times after infection. Both transcriptome and immunohistochemical analysis revealed a downregulation of surfactant proteins in SARS-CoV-2-infected alveolospheres. Interestingly, these findings are in line with previous observations of surfactant protein downregulation after influenza injury (Kebaabetswe et al., 2015). The loss of surfactant proteins has adverse repercussions for the host, as surfactants are essential for preventing alveolar collapse and for controlling both innate and adaptive immune responses (Crouch and Wright, 2001; McCormack and Whitsett, 2002). Our finding that the type-II IFN pathway is activated in AT2s *ex vivo* is somewhat surprising, as typically it is the IFN-I and IFN-III pathways that are activated in cells by viral infection (Barrat et al., 2019; Bartee et al., 2008). Significantly, these unexpected findings from alveolosphere-derived AT2s mirror responses in AT2s from COVID-19 patient lungs, further supporting the relevance of alveolosphere-derived AT2 for SARS-CoV-2 studies. Our study further provided evidence that pre-treatment with IFNs shows prophylactic effectiveness in alveolospheres. Future studies will reveal whether such a prophylactic effect can provide resistance to viral propagation *in vivo*.

(D) Venn diagram shows enrichment of upregulated transcripts associated with different IFN pathways in AT2s derived from COVID-19 human lungs.
(E) RNA *in situ* hybridization for *SARS-CoV-2* (green) and *SFTPB* (red) on control and COVID-19 lung sections.
(F) Co-immunostaining for SARS-CoV-2 (green), ABCA3 (red) (left); SARS-CoV2 (green) and NKX2-1 (red) (middle); and active caspase-3 (CASP3) (red) (right) on COVID-19 lung sections. DAPI stains nuclei. Scale bars: 20 μm and 60 μm (NKX2-1).
(G) Quantification of SFTPB$^+$ cells, NKX2-1$^+$ cells, and ABCA3$^+$ cells in total SARS-CoV-2$^+$ cells.
(H) Quantification of active CASP3$^+$ cells in total SARS-CoV-2$^+$ cells. Data are presented as mean ± SEM.

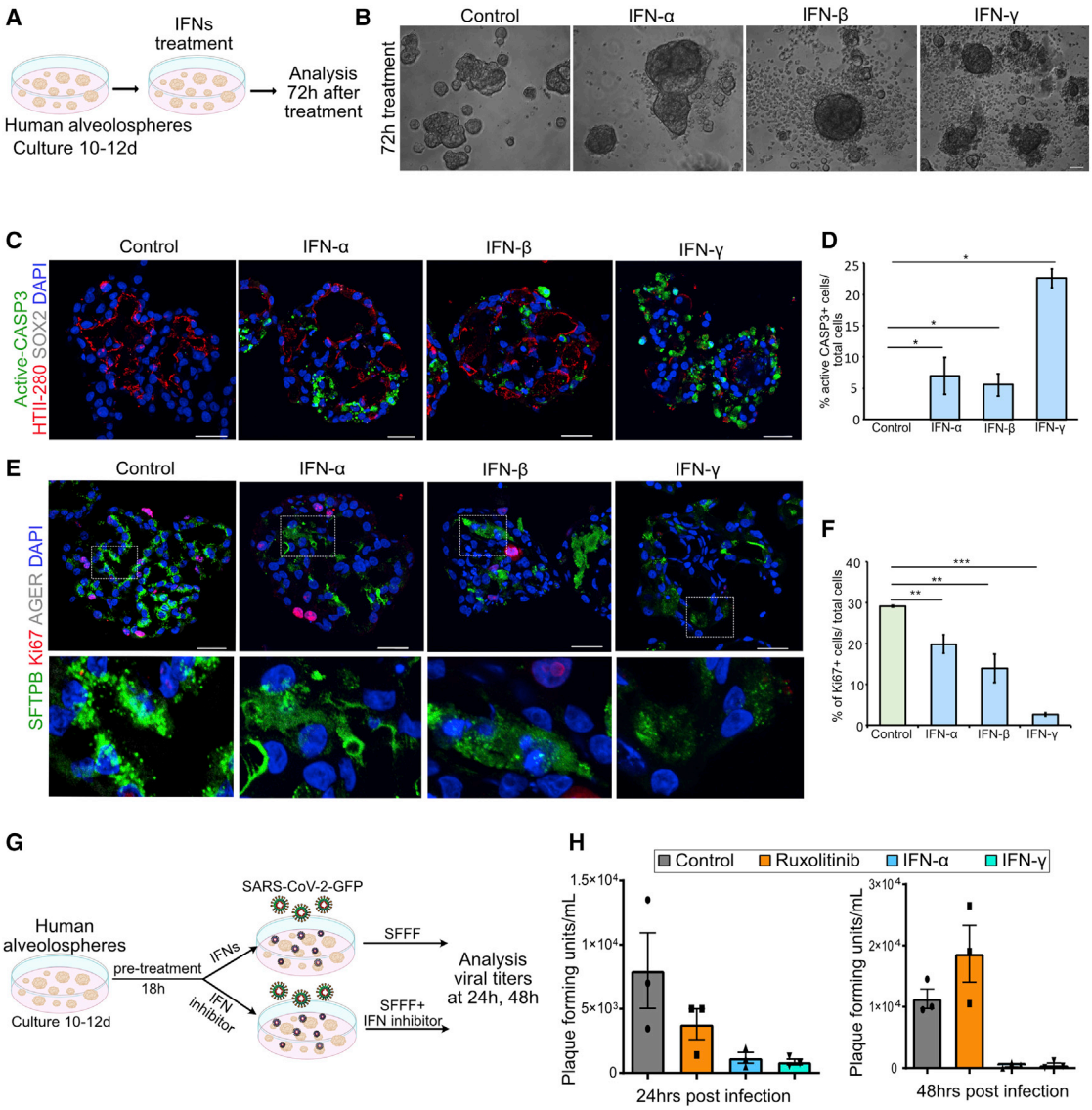

Figure 6. IFN Treatment Recapitulates Features of SARS-CoV-2 Infection Including Cell Death and Loss of Surfactants in Alveolosphere-Derived AT2s

(A) Schematic of experimental design. Human lung alveolospheres were treated with IFNα, IFNβ or IFNγ for 72 h.

(B) Representative images of control and IFNα-, IFNβ-, and IFNγ-treated human lung alveolospheres.

(C) Immunostaining for active-caspase-3 (green), HTII-280 (red), and SOX2 (gray) in control and IFN-treated alveolospheres. DAPI stains nuclei (blue). Scale bar: 30 μm.

(D) Quantification of active caspase-3$^+$ cells in total DAPI$^+$ (per alveolosphere) cells in control and IFN-treated human alveolospheres.

(E) Immunostaining for SFTPB (green), Ki67 (red), and AGER (gray) in controls and IFNα-, IFNβ-, or IFNγ-treated human alveolospheres. DAPI stains nuclei (blue). Scale bar: 30 μm.

(F) Quantification of Ki67$^+$ cells in total DAPI$^+$ cells in control and IFN-treated human alveolospheres. *$p < 0.05$; **$p < 0.01$; ***$p < 0.001$.

(G) Schematic of IFNs or IFN inhibitor treatment followed by SARS-CoV-2 infection.

(H) Viral titers in control (gray), ruxolitinib-treated (orange), IFNα-treated (blue), and IFNγ-treated (green) cultures were determined by plaque assay using media collected from alveolosphere cultures at 24 and 48 h post-infection. Data are presented as mean ± SEM.

There are several reasons why AT2s grown in alveolosphere cultures are preferred over the currently used cell lines, such as Calu-3, A549, Vero, and H1299. For example, A549 cells derived from a human lung adenocarcinoma have been widely used as surrogates for alveolar epithelial cells in viral infection studies (Hoffmann et al., 2020; Letko et al., 2020; Osada et al., 2014; Ujie et al., 2019). However, the A549 cell line lacks the cardinal features of lung epithelial cells, including the ability to form epithelial tight junctions; they also harbor numerous genetic alterations (Mason and Williams, 1980; Osada et al., 2014). More importantly, A549 cells do not express the SARS-CoV-2 receptor ACE2, and viral infection studies rely on the ectopic expression

of this receptor (Blanco-Melo et al., 2020). Accordingly, transformed cell lines do not faithfully recapitulate the native lung epithelial cells (Mason and Williams, 1980). In contrast, AT2-based alveolospheres are highly polarized epithelial structures that retain molecular and morphological features and maintain the ability to differentiate into AT1s under suitable conditions.

Other models, including AT2s derived from directed differentiation of induced pluripotent stem cells (iPSCs), can serve as alternative models for *ex vivo* studies (Jacob et al., 2017; Yamamoto et al., 2017). Indeed, recent studies using primary stem cells and iPSC-derived 3D cultures from lung, brain, kidney, and intestine have provided insights into SARS-CoV-2 cell tropism, viral replication kinetics, factors that promote viral entry, and the associated cellular responses (Huang et al., 2020b; Jacob et al., 2020; Lamers et al., 2020; Monteil et al., 2020; Ramani et al., 2020; Yang et al., 2020). Furthermore, such models have been useful for the discovery of anti-viral drugs as well as preclinical humanized *ex vivo* models to test the efficacy of existing therapeutically relevant molecules (Monteil et al., 2020; Yang et al., 2020). Consistent with our data, a recent study using iPSC-derived AT2s (iAT2s) uncovered epithelial intrinsic inflammatory responses, including IFN pathways, after SARS-CoV-2 infection (Huang et al., 2020b). Despite these similarities, primary lung stem cell-derived models and iPSC-derived iAT2 models have their unique advantages and disadvantages. For example, although iPSC-derived models are more conducive to genetic modulation, they may not be suitable for studying age-specific phenomena. This is particularly important in the case of severe COVID-19, as this disease is more severe in aged than in younger populations and the cellular responses to infection may differ in adolescents compared to the elderly (Muus et al., 2020; Ziegler et al., 2020). Nevertheless, human stem cell-based models will be very valuable for rapid and scalable disease modeling and drug discovery.

One limitation of alveolosphere models in general is that they lack the complete cellular complexity of native tissues. However, such simplified models also offer several advantages. First, as has already been demonstrated here, they serve as an excellent model to study intrinsic cellular mechanisms that are triggered in response to viruses and other pathogens. For example, our study identified numerous IFN ligands and target genes that are activated by AT2s in response to SARS-CoV-2 infection. Second, our study found that AT2s activate type II IFN signaling in the absence of *IFNG* ligands, suggesting the possibility of unknown non-canonical type II ligands. As discussed above, currently used cancer cell lines, e.g., Vero cells and A549 cells, are defective in their responses to certain IFN pathways (Blanco-Melo et al., 2020; Desmyter et al., 1968; Osada et al., 2014) and, therefore, are not suitable for studying IFN signaling. As we demonstrated here, alveolosphere-derived AT2s express receptors and downstream components needed for IFN signal transduction. Therefore, alveolosphere-derived AT2s offer a faithful model that recapitulates *in vivo* cellular contexts for studying and identifying components that are either specific or shared between different classes of IFN signaling. Third, although not tested here, alveolosphere-derived AT2s can be combined with other cell types, e.g., specific immune cell subsets, to study the interactions between AT2s and immune cells in the presence and absence of pathogens, such as SARS-CoV-2. Indeed, such efforts were made in the context of tumor-immune cell interactions (Neal et al., 2018).

In conclusion, we provide chemically defined and modular culture conditions for the selective expansion and differentiation of AT2s that retain the cardinal features of AT2s, including the ability to self-renew, produce surfactants, and differentiate into AT1s. SARS-CoV-2 infection of the defined AT2 alveolosphere system revealed an induction of autocrine and presumed paracrine IFN signaling and inflammatory pathways that blocked surfactant production and proliferation and induced cell death. This newly developed alveolosphere model offers a unique system for studying SARS-CoV-2 infection and developing effective therapies for COVID-19 and other respiratory diseases.

Limitations of Study

Human lung tissue specimens used for generating alveolospheres came from healthy donors from different age groups. Our study has not taken into account the differences in tissue composition or cell behavior among different age groups. Future studies will need to consider these variables in studying the properties of AT2 cells in 3D cultures. Similarly, the affect age on viral infection and the associated responses were not accounted in our study. Although the AT2 expansion medium is completely defined, AT2 differentiation medium currently uses human serum. Development of a defined AT2 differentiation medium will be valuable for genetic and pharmacological screenings and will most likely advance the use of alveolospheres for cell-based therapies.

STAR★METHODS

Detailed methods are provided in the online version of this paper and include the following:

- KEY RESOURCES TABLE
- RESOURCE AVAILABILITY
  - Lead Contact
  - Materials Availability
  - Data and Code Availability
- EXPERIMENTAL MODEL AND SUBJECT DETAILS
  - Animal Studies
  - Human lung tissue
  - Human COVID-19 infected subjects
- METHOD DETAILS
  - Mouse lung tissue dissociation
  - Human lung tissue dissociation
  - Isolation of human and mouse AT2s
  - Alveolosphere culture
  - Alveolosphere passaging
  - AT2 differentiation
  - Cell culture and SARS-CoV-2 Virus Propagation
  - Alveolosphere infection experiment for bulk RNaseq and qPCR studies
  - Infection of AT2 alveolospheres with SARS-CoV-2
  - Interferon treatment
  - Alveolospheres fixation and sectioning
  - Immunostaining on COVID-19 lungs
  - Immunostaining on alveolospheres
  - RNA *in situ* hybridization
  - Image acquisition, processing and quantification

SUPPLEMENTAL INFORMATION

Supplemental Information can be found online at https://doi.org/10.1016/j.stem.2020.10.005.

ACKNOWLEDGMENTS

We thank Brigid Hogan for advice and critical reading of the manuscript. We thank Peiying Shan (Yale University) and Randell lab members (University of North Carolina at Chapel Hill) for human lung preparation, the Duke Cancer Institute Flow Cytometry Shared Resource for cell sorting, the Duke University Light Microscopy Core Facility for imaging equipment and consultation, and the Duke Compute Cluster for help with computing sequencing data. This work was performed in part at the Duke University Shared Materials Instrumentation Facility, a member of the North Carolina Research Triangle Nanotechnology Network, which is supported by the National Science Foundation (grant ECCS-1542015) as part of the National Nanotechnology Coordinated Infrastructure. SARS-Related Coronavirus 2, Isolate USA-WA1/2020, NR-52281 was deposited by the Centers for Disease Control and Prevention and obtained through BEI Resources, NIAID, NIH. Biocontainment work was performed in the Duke Regional Biocontainment Laboratory, which received partial support for construction from the National Institutes of Health, National Institute of Allergy and Infectious Diseases (UC6-AI058607). Y.K. is a fellow of the Japan Society for the Promotion of Science Overseas Research. V.S. is supported by a fellowship from Regeneration Next Initiative at Duke University. A.K. is supported by a medical scientist training program fellowship from NHLBI/NIH (F30HL143911). S.H.R. is supported by Cystic Fibrosis Foundation grant BOUCHE15R0 and NIH grant DK065988. This work was supported by a generous gift from the Chan Zuckerberg Foundation and NIH grants AI132178 and AI149644 to R.S.B. This work was supported by NHLBI/NIH (R00HL127181, R01HL146557, and R01HL153375), NIGMS (R21GM1311279), and funds from Regeneration NeXT and Kaganov-MEDx Pulmonary Research Initiative at Duke University to P.R.T. This work was partially supported by a grant from the United Therapeutics Corporation (to P.R.T.). P.R.T. is a Whitehead Scholar at Duke University.

AUTHOR CONTRIBUTIONS

H.K. designed and optimized alveolosphere cultures, analyzed the data, and edited manuscript. V.S. designed and optimized alveolosphere cultures and co-wrote the manuscript. A.T. performed alveolosphere cultures, histology, and immunostainings; analyzed the data; and co-wrote the manuscript. Y.K. designed and performed scRNA-seq, bulk RNA-seq, RT-PCR, and computational analysis and co-wrote the manuscript. C.E.E., E.J.F., and B.E.H. performed viral infections. A.K. provided reagents. T.A. and Y.M. performed stainings and quantification on COVID-19 lung sections. P.J.L. and S.H.R. provided human lung tissues. R.C.B., N.S.H., and R.S.B. contributed reagents and recombinant viruses. P.R.T. designed, conceived, and supervised the work and co-wrote the manuscript. All authors reviewed and edited the manuscript.

DECLARATION OF INTERESTS

A patent application (PCT/US20/53158) related to this work has been filed. H.K. and P.R.T. are listed as co-inventors on this application. P.R.T. serves as a consultant for Cellarity and Surrozen.

Received: June 17, 2020
Revised: August 17, 2020
Accepted: October 13, 2020
Published: October 21, 2020

REFERENCES

Arenkiel, B.R., Hasegawa, H., Yi, J.J., Larsen, R.S., Wallace, M.L., Philpot, B.D., Wang, F., and Ehlers, M.D. (2011). Activity-induced remodeling of olfactory bulb microcircuits revealed by monosynaptic tracing. PLoS One *6*, e29423.

Barkauskas, C.E., Cronce, M.J., Rackley, C.R., Bowie, E.J., Keene, D.R., Stripp, B.R., Randell, S.H., Noble, P.W., and Hogan, B.L.M. (2013). Type 2 alveolar cells are stem cells in adult lung. J. Clin. Invest. *123*, 3025–3036.

Barkauskas, C.E., Chung, M.-I., Fioret, B., Gao, X., Katsura, H., and Hogan, B.L.M. (2017). Lung organoids: current uses and future promise. Development *144*, 986–997.

Barrat, F.J., Crow, M.K., and Ivashkiv, L.B. (2019). Interferon target-gene expression and epigenomic signatures in health and disease. Nat. Immunol. *20*, 1574–1583.

Bartee, E., Mohamed, M.R., and McFadden, G. (2008). Tumor necrosis factor and interferon: cytokines in harmony. Curr. Opin. Microbiol. *11*, 378–383.

Blanco-Melo, D., Nilsson-Payant, B.E., Liu, W.-C., Møller, R., Panis, M., Sachs, D., Albrecht, R.A., and tenOever, B.R. (2020). SARS-CoV-2 launches a unique transcriptional signature from in vitro, ex vivo, and in vivo systems. bioRxiv. https://doi.org/10.1101/2020.03.24.004655.

Bolger, A.M., Lohse, M., and Usadel, B. (2014). Trimmomatic: a flexible trimmer for Illumina sequence data. Bioinformatics *30*, 2114–2120.

Bost, P., Giladi, A., Liu, Y., Bendjelal, Y., Xu, G., David, E., Blecher-Gonen, R., Cohen, M., Medaglia, C., Li, H., et al. (2020). Host-Viral Infection Maps Reveal Signatures of Severe COVID-19 Patients. Cell *181*, 1475–1488.e12.

Bradley, B.T., Maioli, H., Johnston, R., Chaudhry, I., Fink, S.L., Xu, H., Najafian, B., Marshall, D., Lacy, J.M., Williams, T., et al. (2020). Histopathology and Ultrastructural Findings of Fatal COVID-19 Infections. medRxiv. https://doi.org/10.1101/2020.04.17.20058545.

Chung, M.-I., Bujnis, M., Barkauskas, C.E., Kobayashi, Y., and Hogan, B.L.M. (2018). Niche-mediated BMP/SMAD signaling regulates lung alveolar stem cell proliferation and differentiation. Development *145*, dev163014.

Clementi, N., Ferrarese, R., Criscuolo, E., Diotti, R.A., Castelli, M., Scagnolari, C., Burioni, R., Antonelli, G., Clementi, M., and Mancini, N. (2020). Interferon-β-1a Inhibition of Severe Acute Respiratory Syndrome-Coronavirus 2 In Vitro When Administered After Virus Infection. J. Infect. Dis. *222*, 722–725.

Crouch, E., and Wright, J.R. (2001). Surfactant proteins a and d and pulmonary host defense. Annu. Rev. Physiol. *63*, 521–554.

Desmyter, J., Melnick, J.L., and Rawls, W.E. (1968). Defectiveness of interferon production and of rubella virus interference in a line of African green monkey kidney cells (Vero). J. Virol. *2*, 955–961.

Drost, J., and Clevers, H. (2018). Organoids in cancer research. Nat. Rev. Cancer *18*, 407–418.

Dye, B.R., Hill, D.R., Ferguson, M.A.H., Tsai, Y.-H., Nagy, M.S., Dyal, R., Wells, J.M., Mayhew, C.N., Nattiv, R., Klein, O.D., et al. (2015). In vitro generation of human pluripotent stem cell derived lung organoids. eLife *4*, e05098.

Felgenhauer, U., Schoen, A., Gad, H.H., Hartmann, R., Schaubmar, A.R., Failing, K., Drosten, C., and Weber, F. (2020). Inhibition of SARS-CoV-2 by type I and type III interferons. J. Biol. Chem. *295*, 13958–13964.

Gonzalez, R.F., Allen, L., Gonzales, L., Ballard, P.L., and Dobbs, L.G. (2010). HTII-280, a biomarker specific to the apical plasma membrane of human lung alveolar type II cells. J. Histochem. Cytochem. *58*, 891–901.

Habermann, A.C., Gutierrez, A.J., Bui, L.T., Yahn, S.L., Winters, N.I., Calvi, C.L., Peter, L., Chung, M.-I., Taylor, C.J., Jetter, C., et al. (2019). Single-cell RNA-sequencing reveals profibrotic roles of distinct epithelial and mesenchymal lineages in pulmonary fibrosis. bioRxiv. https://doi.org/10.1101/753806.

Hafemeister, C., and Satija, R. (2019). Normalization and variance stabilization of single-cell RNA-seq data using regularized negative binomial regression. bioRxiv. https://doi.org/10.1101/576827.

Hoffmann, M., Kleine-Weber, H., Schroeder, S., Krüger, N., Herrler, T., Erichsen, S., Schiergens, T.S., Herrler, G., Wu, N.-H., Nitsche, A., et al. (2020). SARS-CoV-2 Cell Entry Depends on ACE2 and TMPRSS2 and Is Blocked by a Clinically Proven Protease Inhibitor. Cell *181*, 271–280.e8.

Hogan, B., and Tata, P.R. (2019). Cellular organization and biology of the respiratory system. Nat. Cell Biol. https://doi.org/10.1038/s41556-019-0357-7.

Hou, Y.J., Okuda, K., Edwards, C.E., Martinez, D.R., Asakura, T., Dinnon, K.H., Kato, T., Lee, R.E., Yount, B.L., Mascenik, T.M., et al. (2020). SARS-CoV-2 Reverse Genetics Reveals a Variable Infection Gradient in the Respiratory Tract. Cell *182*, 429–446.e14.

Hu, H., Gehart, H., Artegiani, B., LÖpez-Iglesias, C., Dekkers, F., Basak, O., van Es, J., Chuva de Sousa Lopes, S.M., Begthel, H., Korving, J., et al. (2018). Long-Term Expansion of Functional Mouse and Human Hepatocytes as 3D Organoids. Cell *175*, 1591–1606.e19.

Huang, C., Wang, Y., Li, X., Ren, L., Zhao, J., Hu, Y., Zhang, L., Fan, G., Xu, J., Gu, X., et al. (2020a). Clinical features of patients infected with 2019 novel coronavirus in Wuhan, China. Lancet *395*, 497–506.

Huang, J., Hume, A.J., Abo, K.M., Werder, R.B., Villacorta-Martin, C., Alysandratos, K.-D., Beermann, M.L., Simone-Roach, C., Lindstrom-Vautrin, J., Olejnik, J., et al. (2020b). SARS-CoV-2 Infection of Pluripotent Stem Cell-Derived Human Lung Alveolar Type 2 Cells Elicits a Rapid Epithelial-Intrinsic Inflammatory Response. Cell Stem Cell. https://doi.org/10.1016/j.stem.2020.09.013.

Huch, M., Dorrell, C., Boj, S.F., van Es, J.H., Li, V.S.W., van de Wetering, M., Sato, T., Hamer, K., Sasaki, N., Finegold, M.J., et al. (2013). In vitro expansion of single Lgr5+ liver stem cells induced by Wnt-driven regeneration. Nature *494*, 247–250.

Jacob, A., Morley, M., Hawkins, F., McCauley, K.B., Jean, J.C., Heins, H., Na, C.-L., Weaver, T.E., Vedaie, M., Hurley, K., et al. (2017). Differentiation of Human Pluripotent Stem Cells into Functional Lung Alveolar Epithelial Cells. Cell Stem Cell *21*, 472–488.e10.

Jacob, F., Pather, S.R., Huang, W.-K., Zhang, F., Wong, S.Z.H., Zhou, H., Cubitt, B., Fan, W., Chen, C.Z., Xu, M., et al. (2020). Human Pluripotent Stem Cell-Derived Neural Cells and Brain Organoids Reveal SARS-CoV-2 Neurotropism Predominates in Choroid Plexus Epithelium. Cell Stem Cell. https://doi.org/10.1016/j.stem.2020.09.016.

Katsura, H., Kobayashi, Y., Tata, P.R., and Hogan, B.L.M. (2019). IL-1 and TNFα Contribute to the Inflammatory Niche to Enhance Alveolar Regeneration. Stem Cell Reports *12*, 657–666.

Kebaabetswe, L.P., Haick, A.K., Gritsenko, M.A., Fillmore, T.L., Chu, R.K., Purvine, S.O., Webb-Robertson, B.-J., Matzke, M.M., Smith, R.D., Waters, K.M., et al. (2015). Proteomic analysis reveals down-regulation of surfactant protein B in murine type II pneumocytes infected with influenza A virus. Virology *483*, 96–107.

Kim, D., Paggi, J.M., Park, C., Bennett, C., and Salzberg, S.L. (2019). Graph-based genome alignment and genotyping with HISAT2 and HISAT-genotype. Nat. Biotechnol. *37*, 907–915.

Koerner, I., Kochs, G., Kalinke, U., Weiss, S., and Staeheli, P. (2007). Protective role of beta interferon in host defense against influenza A virus. J. Virol. *81*, 2025–2030.

Kuleshov, M.V., Jones, M.R., Rouillard, A.D., Fernandez, N.F., Duan, Q., Wang, Z., Koplev, S., Jenkins, S.L., Jagodnik, K.M., Lachmann, A., et al. (2016). Enrichr: a comprehensive gene set enrichment analysis web server 2016 update. Nucleic Acids Res. *44*, W90–W97.

Lamers, M.M., Beumer, J., van der Vaart, J., Knoops, K., Puschhof, J., Breugem, T.I., Ravelli, R.B.G., Paul van Schayck, J., Mykytyn, A.Z., Duimel, H.Q., et al. (2020). SARS-CoV-2 productively infects human gut enterocytes. Science *369*, 50–54.

Lancaster, M.A., and Huch, M. (2019). Disease modelling in human organoids. Dis. Model. Mech. *12*, dmm039347.

Lancaster, M.A., and Knoblich, J.A. (2014). Organogenesis in a dish: modeling development and disease using organoid technologies. Science *345*, 1247125.

Lee, J.-H., Kim, J., Gludish, D., Roach, R.R., Saunders, A.H., Barrios, J., Woo, A.J., Chen, H., Conner, D.A., Fujiwara, Y., et al. (2013). Surfactant protein-C chromatin-bound green fluorescence protein reporter mice reveal heterogeneity of surfactant protein C-expressing lung cells. Am. J. Respir. Cell Mol. Biol. *48*, 288–298.

Letko, M., Marzi, A., and Munster, V. (2020). Functional assessment of cell entry and receptor usage for SARS-CoV-2 and other lineage B betacoronaviruses. Nat. Microbiol. *5*, 562–569.

Li, H., Handsaker, B., Wysoker, A., Fennell, T., Ruan, J., Homer, N., Marth, G., Abecasis, G., and Durbin, R.; 1000 Genome Project Data Processing Subgroup (2009). The Sequence Alignment/Map format and SAMtools. Bioinformatics *25*, 2078–2079.

Liao, Y., Smyth, G.K., and Shi, W. (2014). featureCounts: an efficient general purpose program for assigning sequence reads to genomic features. Bioinformatics *30*, 923–930.

Liao, M., Liu, Y., Yuan, J., Wen, Y., Xu, G., Zhao, J., Cheng, L., Li, J., Wang, X., Wang, F., et al. (2020). Single-cell landscape of bronchoalveolar immune cells in patients with COVID-19. Nat. Med. *26*, 842–844.

Love, M.I., Huber, W., and Anders, S. (2014). Moderated estimation of fold change and dispersion for RNA-seq data with DESeq2. Genome Biol. *15*, 550.

Macosko, E.Z., Basu, A., Satija, R., Nemesh, J., Shekhar, K., Goldman, M., Tirosh, I., Bialas, A.R., Kamitaki, N., Martersteck, E.M., et al. (2015). Highly Parallel Genome-wide Expression Profiling of Individual Cells Using Nanoliter Droplets. Cell *161*, 1202–1214.

Martin, M. (2011). Cutadapt removes adapter sequences from high-throughput sequencing reads. EMBnet. J. *17*, 10–12.

Mason, R.J., and Williams, M.C. (1980). Phospholipid composition and ultrastructure of A549 cells and other cultured pulmonary epithelial cells of presumed type II cell origin. Biochim. Biophys. Acta *617*, 36–50.

McCormack, F.X., and Whitsett, J.A. (2002). The pulmonary collectins, SP-A and SP-D, orchestrate innate immunity in the lung. J. Clin. Invest. *109*, 707–712.

McQualter, J.L., Yuen, K., Williams, B., and Bertoncello, I. (2010). Evidence of an epithelial stem/progenitor cell hierarchy in the adult mouse lung. Proc. Natl. Acad. Sci. USA *107*, 1414–1419.

Menachery, V.D., Eisfeld, A.J., Schäfer, A., Josset, L., Sims, A.C., Proll, S., Fan, S., Li, C., Neumann, G., Tilton, S.C., et al. (2014). Pathogenic influenza viruses and coronaviruses utilize similar and contrasting approaches to control interferon-stimulated gene responses. mBio *5*, e01174, e14.

Monteil, V., Kwon, H., Prado, P., Hagelkrüys, A., Wimmer, R.A., Stahl, M., Leopoldi, A., Garreta, E., Hurtado Del Pozo, C., Prosper, F., et al. (2020). Inhibition of SARS-CoV-2 Infections in Engineered Human Tissues Using Clinical-Grade Soluble Human ACE2. Cell *181*, 905–913.e7.

Muus, C., Luecken, M.D., Eraslan, G., Waghray, A., Heimberg, G., Sikkema, L., Kobayashi, Y., Vaishnav, E.D., Subramanian, A., Smilie, C., et al. (2020). Integrated analyses of single-cell atlases reveal age, gender, and smoking status associations with cell type-specific expression of mediators of SARS-CoV-2 viral entry and highlights inflammatory programs in putative target cells. bioRxiv, 2020.04.19.049254.

Neal, J.T., Li, X., Zhu, J., Giangarra, V., Grzeskowiak, C.L., Ju, J., Liu, I.H., Chiou, S.-H., Salahudeen, A.A., Smith, A.R., et al. (2018). Organoid Modeling of the Tumor Immune Microenvironment. Cell *175*, 1972–1988.e16.

Nikolić, M.Z., Sun, D., and Rawlins, E.L. (2018). Human lung development: recent progress and new challenges. Development *145*, dev163485.

Osada, N., Kohara, A., Yamaji, T., Hirayama, N., Kasai, F., Sekizuka, T., Kuroda, M., and Hanada, K. (2014). The genome landscape of the african green monkey kidney-derived vero cell line. DNA Res. *21*, 673–683.

Peng, W.C., Logan, C.Y., Fish, M., Anbarchian, T., Aguisanda, F., Álvarez-Varela, A., Wu, P., Jin, Y., Zhu, J., Li, B., et al. (2018). Inflammatory Cytokine TNFα Promotes the Long-Term Expansion of Primary Hepatocytes in 3D Culture. Cell *175*, 1607–1619.e15.

Platanias, L.C. (2005). Mechanisms of type-I- and type-II-interferon-mediated signalling. Nat. Rev. Immunol. *5*, 375–386.

Ramani, A., Müller, L., Ostermann, P.N., Gabriel, E., Abida-Islam, P., Müller-Schiffmann, A., Mariappan, A., Goureau, O., Gruell, H., Walker, A., et al. (2020). SARS-CoV-2 targets neurons of 3D human brain organoids. EMBO J. *39*, e106230.

Rock, J.R., Barkauskas, C.E., Cronce, M.J., Xue, Y., Harris, J.R., Liang, J., Noble, P.W., and Hogan, B.L.M. (2011). Multiple stromal populations contribute to pulmonary fibrosis without evidence for epithelial to mesenchymal transition. Proc. Natl. Acad. Sci. USA *108*, E1475–E1483.

Shiraishi, K., Shichino, S., Ueha, S., Nakajima, T., Hashimoto, S., Yamazaki, S., and Matsushima, K. (2019a). Mesenchymal-Epithelial Interactome Analysis Reveals Essential Factors Required for Fibroblast-Free Alveolosphere Formation. iScience *11*, 318–333.

Shiraishi, K., Nakajima, T., Shichino, S., Deshimaru, S., Matsushima, K., and Ueha, S. (2019b). In vitro expansion of endogenous human alveolar epithelial type II cells in fibroblast-free spheroid culture. Biochem. Biophys. Res. Commun. *515*, 579–585.

Stuart, T., Butler, A., Hoffman, P., Hafemeister, C., Papalexi, E., Mauck, W.M., 3rd, Hao, Y., Stoeckius, M., Smibert, P., and Satija, R. (2019). Comprehensive Integration of Single-Cell Data. Cell *177*, 1888–1902.e21.

Sungnak, W., Huang, N., Bécavin, C., Berg, M., Queen, R., Litvinukova, M., Talavera-López, C., Maatz, H., Reichart, D., Sampaziotis, F., et al. (2020). SARS-CoV-2 entry factors are highly expressed in nasal epithelial cells together with innate immune genes. Nat. Med. *26*, 681–687.

Syedbasha, M., and Egli, A. (2017). Interferon Lambda: Modulating Immunity in Infectious Diseases. Front. Immunol. *8*, 119.

Takashima, S., Martin, M.L., Jansen, S.A., Fu, Y., Bos, J., Chandra, D., O'Connor, M.H., Mertelsmann, A.M., Vinci, P., Kuttiyara, J., et al. (2019). T cell-derived interferon-γ programs stem cell death in immune-mediated intestinal damage. Sci. Immunol. *4*, eaay8556.

Ujie, M., Takada, K., Kiso, M., Sakai-Tagawa, Y., Ito, M., Nakamura, K., Watanabe, S., Imai, M., and Kawaoka, Y. (2019). Long-term culture of human lung adenocarcinoma A549 cells enhances the replication of human influenza A viruses. J. Gen. Virol. *100*, 1345–1349.

Velasco, S., Kedaigle, A.J., Simmons, S.K., Nash, A., Rocha, M., Quadrato, G., Paulsen, B., Nguyen, L., Adiconis, X., Regev, A., et al. (2019). Individual brain organoids reproducibly form cell diversity of the human cerebral cortex. Nature *570*, 523–527.

Weiner, A.I., Jackson, S.R., Zhao, G., Quansah, K.K., Farshchian, J.N., Neupauer, K.M., Littauer, E.Q., Paris, A.J., Liberti, D.C., Scott Worthen, G., et al. (2019). Mesenchyme-free expansion and transplantation of adult alveolar progenitor cells: steps toward cell-based regenerative therapies. NPJ Regen. Med. *4*, 17.

Wu, Z., and McGoogan, J.M. (2020). Characteristics of and Important Lessons From the Coronavirus Disease 2019 (COVID-19) Outbreak in China: Summary of a Report of 72 314 Cases From the Chinese Center for Disease Control and Prevention. JAMA *323*, 1239–1242.

Yamamoto, Y., Gotoh, S., Korogi, Y., Seki, M., Konishi, S., Ikeo, S., Sone, N., Nagasaki, T., Matsumoto, H., Muro, S., et al. (2017). Long-term expansion of alveolar stem cells derived from human iPS cells in organoids. Nat. Methods *14*, 1097–1106.

Yang, L., Han, Y., Nilsson-Payant, B.E., Gupta, V., Wang, P., Duan, X., Tang, X., Zhu, J., Zhao, Z., Jaffré, F., et al. (2020). A Human Pluripotent Stem Cell-based Platform to Study SARS-CoV-2 Tropism and Model Virus Infection in Human Cells and Organoids. Cell Stem Cell *27*, 125–136.e7.

Zacharias, W.J., Frank, D.B., Zepp, J.A., Morley, M.P., Alkhaleel, F.A., Kong, J., Zhou, S., Cantu, E., and Morrisey, E.E. (2018). Regeneration of the lung alveolus by an evolutionarily conserved epithelial progenitor. Nature *555*, 251–255.

Zhu, N., Zhang, D., Wang, W., Li, X., Yang, B., Song, J., Zhao, X., Huang, B., Shi, W., Lu, R., et al. (2020). A Novel Coronavirus from Patients with Pneumonia in China, 2019. N. Engl. J. Med. *382*, 727–733.

Ziegler, C.G.K., Allon, S.J., Nyquist, S.K., Mbano, I.M., Miao, V.N., Tzouanas, C.N., Cao, Y., Yousif, A.S., Bals, J., Hauser, B.M., et al. (2020). SARS-CoV-2 Receptor ACE2 Is an Interferon-Stimulated Gene in Human Airway Epithelial Cells and Is Detected in Specific Cell Subsets across Tissues. Cell *181*, 1016–1035.e19.

STAR★METHODS

KEY RESOURCES TABLE

REAGENT or RESOURCE	SOURCE	IDENTIFIER
Antibodies		
Rabbit Polyclonal anti-Prosurfactant protein C	Millipore	Cat# ab3786, RRID:AB_91588
Anti-ABCA3	Seven Hills Bioreagents	Cat# WMAB-17G524
Monoclonal Rat anti-RAGE/AGER	R&D systems	Cat# MAB1179, RRID:AB_2289349
Polyclonal Goat Human RAGE/AGER	R&D systems	Cat# AF1145, RRID:AB_354628
Rat Monoclonal anti-Ki67	Thermo Fisher Scientific	Cat# 14-5698-82, RRID: AB_10854564
Mouse Monoclonal anti-HTII-280	Terrace Biotech	Cat# TB-27AHT2-280
Rat monoclonal anti-DC-Lamp	Novus Biologicals	Cat# DDX0191P RRID: AB_2827532
Rabbit Polyclonal anti-SFTPB	Thermo Fisher Scientific	Cat# PA5-42000 RRID: AB_2609628
Mouse Monoclonal anti-SFTPB	Thermo Fisher Scientific	MA1-204 RRID: AB_2633311
Rabbit polyclonal anti-ACE2	Sino biological	Cat# 10108-H31H
Mouse Monoclonal anti-ACE2	R&D systems	Cat# MAB933-SP RRID: AB_2223153
Mouse Monoclonal anti-TMPRSS2	Santa Cruz Biotechnology	Cat# sc-515727 RRID: AB_10863728
Rabbit monoclonal anti-TMPRSS2	Abcam	Cat# ab109131 RRID: AB_10863728
Mouse Monoclonal anti- SARS-CoV/ SARS-CoV-2	Genetex	Cat# GTX632604
Rabbit polyclonal anti- SARS-CoV/ Coronavirus Nucleocapsid	Thermo Fisher Scientific	Cat# PA1-41098 RRID: AB_1087200
Rabbit monoclonal anti- Active Caspase-3	BD Biosciences	Cat# 559565 RRID: AB_397274
Rabbit polyclonal anti-p63	Genetex	Cat# GTX102425 RRID: AB_1952344
Goat-anti-SOX2	R&D systems	Cat# AF2018 RRID: AB_355110
Rabbit monoclonal Anti-TTF1/NKX2-1	Abcam	Cat# ab76013 RRID: AB_1310784
Goat polyclonal Anti-Scgb1a1	Santa Cruz Biotechnology	Cat# sc-9772 RRID: AB_2238819
Mouse Monoclonal Anti-Human EPCAM-488	BioLegend	Cat# 324209 RRID: AB_756083
Rabbit Polyclonal ZO-1	Abcam	Cat# ab216880
Mouse SARS antiserum	Hou et al., 2020	N/A
Alexa Flour 488 goat anti-mouse IgM	Thermo Fisher Scientific	Cat# 10680 RRID: AB_10892893
Alexa Fluor 546 goat anti-hamster IgG	Thermo Fisher Scientific	Cat# A21111, RRID: AB_2535760
Alexa Fluor 594 goat anti-mouse IgG1	Thermo Fisher Scientific	Cat# A21125, RRID:AB_2535767
Alexa Fluor 594 donkey anti-goat IgG	Thermo Fisher Scientific	Cat# A11058, RRID:AB_2534105
Alexa Fluor 647 goat anti-mouse IgG1	Thermo Fisher Scientific	Cat# A21240, RRID:AB_2535809
Alexa Fluor 647 goat anti-rabbit IgG	Thermo Fisher Scientific	Cat# A21245, RRID:AB_2535813
Alexa Fluor 647 donkey anti-mouse IgG	Thermo Fisher Scientific	Cat# A31571, RRID:AB_162542
Mouse-CD31 MicroBeads	Miltenyi Biotec	Cat# 130-097-418 RRID:AB_2814657
Mouse-CD45 MicroBeads	Miltenyi Biotec	Cat# 130-052-301

(*Continued on next page*)

Continued

REAGENT or RESOURCE	SOURCE	IDENTIFIER
Human-CD326 (EpCAM) microbeads	Miltenyi Biotec	Cat# 130-061-101 RRID:AB_2832928
Human TruStain FcX	Biolegend	Cat# 422032
Mouse monoclonal CD326 (EpCAM)	Thermo Fisher Scientific	Cat#14-5791-81
Rat Monoclonal PE anti-mouse CD140a	Biolegend	Cat# 135905
RNAscope® Probe- Hs-SFTPB-C2	ACD	Cat# 544251-C2
RNAscope® Probe- V-nCoV2019-S	ACD	Cat# 848561
Bacterial and Virus Strains		
icSARS-CoV-2-GFP	Hou et al., 2020	GenBank: MT461670
SARS-CoV-2 USA-WA1/2020	(kind gift of Greg Sempowski, Duke University, US)	N/A
Biological Samples		
Human lung tissue	The University of North Carolina at Chapel Hill or Yale University	N/A
Chemicals, Peptides, and Recombinant Proteins		
SB431542	Abcam	Cat# Ab120163
CHIR99021	Tocris	Cat# 4423
BIRB796	Tocris	Cat# 5989
DMH-1	Tocris	Cat# 41-261-0
Heparin	Sigma-Aldrich	Cat# H3149
N-Acetyl-L-cysteine	Sigma-Aldrich	Cat# A9165
Human serum	Sigma-Aldrich	Cat# H4522
Human EGF	GIBCO	Cat# PHG0313
Mouse FGF7	R&D systems	Cat# 5028-KG-025
Mouse FGF10	R&D systems	Cat# 751004
Y27632 2HCl	Selleckchem	Cat# S1049
B-27 Supplement (50X)	Thermo Fisher Scientific	Cat# 17504044
N-2 Supplement (100X)	Thermo Fisher Scientific	Cat# 17502048
Insulin-Transferrin-Selenium (100X)	Thermo Fisher Scientific	Cat# 41400-045
Glutamax	Thermo Fisher Scientific	Cat# 35050061
HEPES (1M)	Thermo Fisher Scientific	Cat# 15630080
Antibiotic-Antimycotic (100X)	Thermo Fisher Scientific	Cat# A5955-100ML
MEM	GIBCO	Cat # 11095
Penicillin/Streptomycin	GIBCO	Cat # 15140
MEM NEAA	GIBCO	Cat# 11140
Human FGF10	BioLegend	Cat# 559304
Mouse IL-1β	BioLegend	Cat# 575104
Human IL-1β	BioLegend	Cat# 579404
Mouse TNFα	BioLegend	Cat# 575204
Mouse Noggin	Peprotech	Cat# 250-38
Human FGF10	BioLegend	Cat# 559304
Human IFNβ	Peprotech	Cat# 300-02BC
Human IFNα	BioLegend	Cat# 592704
Human IFNγ	BioLegend	Cat# 570204
Ruxolitinib	Cayman	Cat# 11609
Tamoxifen	Sigma-Aldrich	Cat# T5648
Dispase	Corning	Cat# 354235
DNase I	Thermo Fisher Scientific	Cat# 10104159001
Collagenase type I	GIBCO	Cat# 17100-017
Matrigel	Corning	Cat# 354230

(*Continued on next page*)

Continued

REAGENT or RESOURCE	SOURCE	IDENTIFIER
Lysotracker	Thermo Fisher Scientific	Cat# L7526
Accutase	Sigma-Aldrich	Cat# A6964
Citrate Buffer, pH 6.0 (10X)	Sigma-Aldrich	Cat# C9999
Fluoromount-G, with DAPI	Thermo Fisher Scientific	Cat# 00-4959
PBS	GIBCO	Cat# 20012027
Sodium bicarbonate	Sigma-Aldrich	Cat# S5761
Sodium hydroxide	Sigma-Aldrich	Cat# S8045
Terra PCR Direct Polymerase	Takara	Cat# 639271
TrypLE Select Enzyme	Thermo Fisher Scientific	Cat# #12563029
TRIzol LS Reagent #11588616	Invitrogen	Cat# 11588616
Direct-zol RNA MicroPrep kit	Zymoresearch	Cat# 11-330M
SuperScript III	Thermo Fisher Scientific	Cat# 18080400
PowerUp SYBR Green Master Mix	Thermo Fisher Scientific	Cat# A25742
NEBNext Poly(A) mRNA Magnetic Isolation Module	New England BioLabs	Cat# E7490
NEBNext Ultra II RNA Library Prep Kit for Illumina	New England BioLabs	Cat# E7770
Thermo Scientific Maxima Reverse Transcriptase (200 U/μL)	Thermo Fisher Scientific	Cat# EP0742
Exonuclease I	New England BioLabs	Cat# M0293
Nextera XT DNA Library Preparation Kit	Illumina	Cat# FC-131-1096
Glutaraldehyde	Sigma	Cat# G5882
Sodium cacodylate buffer pH 7.4	Electron Microscopy Sciences	Cat# 11652
Uranyl acetate	Electron Microscopy Sciences	Cat# 22400
Tannic Acid	Sigma	Cat# 403040
Osmium tetroxide	Electron Microscopy Sciences	Cat# 19180
Propylene oxide	Polysciences	Cat# 00236-1
EMbed 812	Electron Microscopy Sciences	Cat# 14120
Deposited Data		
Raw and analyzed data	This paper	GEO: GSE141634, 152586
Experimental Models: Cell Lines		
N/A		N/A
Experimental Models: Organisms/Strains		
$Sftpc^{tm1(cre/ERT2)Blh}$	Rock et al., 2011	N/A
Rosa26R-CAG-lsl-tdTomato	Arenkiel et al., 2011	N/A
Oligonucleotides		
See Table S3	N/A	N/A
Recombinant DNA		
N/A	N/A	N/A
Software and Algorithms		
dropSeqPipe v0.3	N/A	https://hoohm.github.io/dropSeqPipe
Seurat v3.0.6	Stuart et al., 2019	https://satijalab.org/seurat/
R v3.6.3	N/A	https://www.r-project.org/
R Studio v1.2.5033	N/A	https://rstudio.com/
FastQC v0.11.9	N/A	https://www.bioinformatics.babraham.ac.uk/projects/fastqc/
Cutadapt v1.18	Martin, 2011	https://cutadapt.readthedocs.io/en/stable/
Trimmomatic v0.39	Bolger et al., 2014	http://www.usadellab.org/cms/?page=trimmomatic
HISAT 2.2.0		http://daehwankimlab.github.io/hisat2/
SAMtools v1.9	Li et al., 2009	http://samtools.sourceforge.net/

(*Continued on next page*)

Continued

REAGENT or RESOURCE	SOURCE	IDENTIFIER
Subread v2.0.1	Liao et al., 2014	http://subread.sourceforge.net/
DESeq2	Love et al., 2014	https://bioconductor.org/packages/release/bioc/html/DESeq2.html
EnhancedVolcano v1.5.4	N/A	https://bioconductor.org/packages/release/bioc/html/EnhancedVolcano.html
Enrichr	Kuleshov et al., 2016	https://maayanlab.cloud/Enrichr/
GraphPad Prism 7	Graph Pad	https://www.graphpad.com
FIJI	NIH	https://fiji.sc
Other		
Previously published datasets reanalyzed in this study	GEO	GSE145926, and GSE135893

RESOURCE AVAILABILITY

Lead Contact

Further information and requests for resource/reagents should be directed to and will be fulfilled by the Lead Contact, Purushothama Rao Tata (pt93@duke.edu).

Materials Availability

This study did not generate new unique materials.

Data and Code Availability

RNA-seq data that support the findings of this study have been deposited in the Gene Expression Omnibus (GEO) under accession codes GEO: GSE141634 (MTEC alveolosphere scRNA-seq) and GEO: GSE152586 (Bulk RNA-seq from SARS-CoV-2 infected alveolospheres). Previously published sequencing data that were re-analyzed here are available under accession code GEO: GSE145926 (scRNA-seq data from severe COVID-19 patient lungs) and GEO: GSE135893 (scRNA-seq data from control lungs). All analysis code is available from corresponding author upon request.

EXPERIMENTAL MODEL AND SUBJECT DETAILS

Animal Studies

Mouse strains used in this study were maintained in the C57BL/6 background, including Sftpctm1$^{(cre/ERT2)Blh}$(Sftpc-CreER) (Rock et al., 2011) and Rosa26R-CAG-lsl-tdTomato (Arenkiel et al., 2011) mice were described previously. For lineage labeling, two doses of Tamoxifen (0.2 mg/g body weight, Sigma-Aldrich) was given via Intraperitoneal (IP). All Animal experiments were approved by the Duke University Institutional Animal care and Use Committee. All animals were handled in accordance with the NIH and AAALAC guidelines for humane care and use of laboratory animals. Mice used for experiments were not involved in previous procedures and were drug or test naive. Mice were kept in a SPF breeding area under specified pathogen free conditions. Cages, bedding, food and water were autoclaved. Animals were maintained on the same 12h light/dark cycle and monitored daily by caretakers or researchers. Health monitoring did not reveal any infections in the past 18 months.

Human lung tissue

Excised sub transplant-quality human lung tissues from donors without preexisting chronic lung diseases were obtained from the Marsico Lung Institute at the University of North Carolina at Chapel Hill under the University of North Carolina Biomedical Institutional Review Board-approved protocols (#03-1396) and from Yale University (#0901004626). Informed consent was obtained from all participants where necessary.

Human COVID-19 infected subjects

Tissue blocks or cut sections obtained from three COVID-19 autopsy lungs were obtained from Drs. Ross. E. Zumwalt (University of New Mexico, Albuquerque, NM) and Edana Stroberg (Office of the Chief Medical Examiner, Oklahoma City, OK). Donor demographics are described below. The paraffin blocks were cut to produce 5 μm serial sections for immunofluorescence.

Donor 1. 40-year-old, male. Medical history: Diabetes mellitus. Clinical course: This donor had upper respiratory infection (URI) symptoms three days before he was found dead at home. No intubation occurred. Postmortem testing of the lung was positive for SARS-CoV-2.

Donor 2. 77-year-old, male. Medical history: Acute pancreatitis, acute cholecystitis, and splenectomy. Clinical course: This donor was transferred to the ER because of fever and respiratory distress six days before death. He was dead shortly after arrival. A swab from the nasal cavity and the postmortem lung were positive for SARS-CoV-2.

Donor 3. 91-year-old, female. Medical history: Coronary artery disease, hyperlipidemia, and hypertension. Clinical course: This donor was transferred to the ER because of URI symptoms, hypoxia, weakness, and shortness of breath. A nasal swab was positive for SARS-CoV-2. She was treated with high flow nasal canula, but died from acute pneumonia due to SARS-CoV-2 complicated by an acute hypoxic respiratory failure.

METHOD DETAILS

Mouse lung tissue dissociation

Lung dissociation and FACS were performed as described previously (Chung et al., 2018). Briefly, lungs were intratracheally inflated with 1ml of enzyme solution containing Dispase (5 U/ml), DNase I (0.33U/ml) and Collagenase type I (450 U/ml) in DMEM/F12. Separated lung lobes were diced and incubated with 3ml enzyme solution for 30min at 37°C with rotation. The reaction was quenched with an equal amount of DMEM/F12+10% FBS medium and filtered through a 100μm strainer. The cell pellet was resuspended in red blood cell lysis buffer (100μM EDTA, 10mM KHCO3, 155mM NH4Cl) for 5min, washed with DMEM/F12 containing 10% FBS and filtered through a 40μm strainer. Total cells were centrifuged at 450 g for 5min at 4°C and the cell pellet was processed for AT2 isolation by FACS.

Human lung tissue dissociation

Human lung dissociation was as described previously (Zacharias et al., 2018). Briefly, pleura was removed and remaining human lung tissue (approximately 2g) washed with PBS containing 1% Antibiotic-Antimycotic and cut into small pieces. Visible small airways and blood vessels were carefully removed to avoid clogging. Then samples were digested with 30 mL of enzyme mixture (Collagenase type I: 1.68 mg/ml, Dispase: 5U/ml, DNase: 10U/ml) at 37°C for 1h with rotation. The cells were filtered through a 100μm strainer and rinsed with 15ml DMEM/F12+10% FBS medium through the strainer. The supernatant was removed after centrifugation at 450 g for 10min and the cell pellet was resuspended in red blood cell lysis buffer for 10min, washed with DMEM/F12 containing 10% FBS and filtered through a 40μm strainer. Total cells were centrifuged at 450 g for 5 min at 4°C and the cell pellet was processed for AT2 isolation.

Isolation of human and mouse AT2s

AT2s were isolated by Magnetic-activated cell sorting (MACS) or Fluorescence-activated cell sorting (FACS) based protocols. For mouse AT2 isolation the total lung cell pellet was resuspended in MACS buffer (1x PBS, pH 7.2, 1% BSA, and 2mM EDTA). CD31/CD45 positive cells were depleted using MACS beads according to the manufacturer's instructions. After CD31/CD45 depletion AT2s were sorted based on TdTomato reporter and for AT2s without a reporter, cells were stained using the following antibodies: EpCAM/CD326, PDGFRα/CD140a and Lysotracker as described previously (Katsura et al., 2019). For isolation of human AT2s, approximately 2-10 million total lung cells were resuspended in MACS buffer and incubated with Human TruStain FcX for 15min at 4°C followed by HTII-280 (1:60 dilution) antibody for 1h at 4°C. The cells were washed twice with MACS buffer and then incubated with anti-mouse IgM microbeads for 15min at 4°C. The cells were loaded into the LS column and labeled cells collected magnetically. For FACS based purification of human AT2s, the total lung cell pellet was resuspended in MACS buffer. Cells were positively selected for the EpCAM population using CD326 (EpCAM) microbeads according to the manufacturer's instructions. CD326 selected cells were stained with HTII-280 and LysoTracker at 37°C for 25min followed by secondary Alexa anti-mouse IgM-488 for 10min at 37°C. Sorting was performed using a FACS Vantage SE and SONY SH800S.

Alveolosphere culture

Mouse conventional Alveolosphere culture (using MTEC medium) was performed as described previously (Barkauskas et al., 2013). Briefly, FACS sorted lineage labeled AT2s (1-3 × 10^3) from *Sftpc-CreER; R26R-lsl-tdTomato* mice and PDGFRα$^+$ (5 × 10^4) cells were resuspended in MTEC/Plus or serum free medium and mixed with an equal volume of growth factor-reduced Matrigel.

For feeder free culture, AT2s (1-3 × 10^3) were resuspended in serum free medium and mixed with an equal amount of Matrigel. For drop culture, 3 drops of 50μl of cells-medium/Matrigel mixture were plated in each well of a 6-well plate. The medium was changed every other day. For detailed SFFF and AMM media composition see Table S1. For human alveolosphere culture, HTII-280$^+$ human AT2s (1-3 × 10^3) were resuspended in serum free medium and mixed with an equal amount of Matrigel and plated in 6 well plates. For detailed mouse and human SFFF media composition, see Tables S1 and S2.

Alveolosphere passaging

Mouse alveolosphere passaging experiment was performed in AMM medium, composition as described above. Briefly, FACS sorted mouse AT2s (2 × 10^3) were resuspended in AMM medium and mixed with an equal volume of Matrigel. 3 drops of 50 μl of cells-medium/Matrigel mixture were plated in each well of a 6-well plate for each biological replicate (n = 3). For every passage mouse IL-1β (10ng/ml) was added for the first 4 days and subsequently, the media was replaced with AMM without IL-1β. The medium was changed every three days. Mouse alveolosphere were passaged every 10 days. For human alveolosphere passages, AT2s (3 × 10^3) were resuspended in SFFF medium and mixed with an equal volume of Matrigel. 3 drops of 50μl of cells-medium/Matrigel mixture were plated in each well of a 6-well plate for each donor (n = 3). Alveolospheres were passaged every 10-14 days.

AT2 differentiation

For detailed mouse and human AT2-Differentiation medium (ADM) composition see Tables S1 and S2, respectively. For differentiation, mouse alveolospheres were cultured in AMM for 10 days were switched to AT2-differentiation medium followed by culture for an additional 7 days, except where stated otherwise. For differentiation, human alveolospheres cultured in SFFF media for 10 days were switched to ADM and cultured for an additional 12-15 days, except where stated otherwise. The medium was changed every three days. Human AT2-Differentiation medium contains human serum instead of FBS.

Cell culture and SARS-CoV-2 Virus Propagation

Vero E6 cells were the kind gift of Greg Grey and were maintained at 37°C and 5% CO_2 in MEM supplemented with 1% Penicillin/Streptomycin, 10% FBS, 1mM Sodium Pyruvate, and 1x MEM NEAA. To grow stocks of SARS-CoV-2, Vero E6 cells were inoculated with BEI isolate SARS-CoV-2 USA-WA1/2020 (kind gift of Greg Sempowski) at a MOI 0.01 in viral growth media (MEM supplemented with 1% Pen/Strep, 2% FBS, 1mM Sodium Pyruvate, and 1x MEM NEAA). After 1h incubation at 37°C, viral growth media was added to bring the final volume to 30 ml. Virus was collected after 72 h and titered on Vero E6 cells using 2x MEM and 0.7% Oxoid Agar and standard procedures. Plaques were stained with crystal violet and counted.

Alveolosphere infection experiment for bulk RNaseq and qPCR studies

To infect alveolosphere cultures, cells were washed with 1 mL PBS then virus was added to cells at a MOI of 1. Virus and cells were incubated for 3.5 hours at 37°C after which virus was removed and cell culture media was added. Infection proceeded for 48 or 120 hours and then alveolospheres were washed with PBS, dissociated as described above. Finally, alveolosphere derived cells were stored in Trizol and stored at −80°C.

Infection of AT2 alveolospheres with SARS-CoV-2

Human alveolosphere cultures were briefly washed twice with 500μl 1X PBS. SARS-CoV-2-GFP (icSARS-CoV-2-GFP virus was described previously (Hou et al., 2020). Briefly, seven cDNA fragments covering the entire SARS-CoV-2 WA1 genome were amplified by RT-PCR using PrimeSTAR GXL HiFi DNA polymerase (TaKaRa). Junctions between each fragment contain non-palindromic sites BsaI (GGTCTCN^NNNN) or BsmBI (CGTCTCN^NNNN) with unique four-nucleotide cohesive ends. Fragment E and F contain two BsmBI sites at both termini, while other fragments harbor BsaI sites at the junction. Each fragment was cloned into high-copy vector pUC57 and verified by Sanger sequencing. A silent mutation T15102A was introduced into a conserved region in nsp12 in plasmid D as a genetic marker. GFP was inserted by replacing the ORF7 gene. Cultures were then inoculated with 200μl of $1x10^7$ PFU/ml of icSARS-CoV-2-GFP virus (Hou et al., 2020) or 200μl of 1X PBS for mock cultures. Alveolospheres were allowed to incubate at 37°C supplemented with 5% CO2 for 2h. Following incubation, the inoculum was removed, and alveolosphere cultures were washed three times with 500μl 1X PBS. 1mL of SFFF media was added to each culture. Alveolospheres were incubated at 37°C for 72h, with samples taken every 24h during infection. To sample, 100μl of media was removed. Equal volumes of fresh media were then added to the cultures to replace the sampled volume. Viral titers were ultimately determined after 72h by plaque assay on Vero E6 cells (USAMRIID). Viral plaques were visualized by neutral red staining after 3 days (Hou et al., 2020). For histological analysis alveolospheres were fixed for 7 days in 10% formalin solution followed by 3 washes in PBS.

Interferon treatment

For interferon and cytokine treatment experiment, Human AT2s (2.5×10^4) from P2 or P3 passage were cultured on the surface of matrigel. Prior to the plating of cells 12 well plates were precoated with matrigel (1:1 matrigel and SFFFM mix) for 30min. AT2s were grown in SFFFM without IL-1β for 7 to 10 days to allow the formation of alveolospheres. Alveolospheres were treated with 20ng/ml interferons (IFNα, IFNβ, IFNγ) for 12h or 72h for RNA isolation and quantitative PCR. For histological analysis, Alveolospheres were treated with indicated interferons for 72h. Human alveolosphere cultures were pretreated with 10ng IFNα or 10ng IFNγ for 18h prior to virus infection. For IFN inhibition studies, alveolospheres were treated with 1μM Ruxolitinib throughout the culture time.

Alveolospheres fixation and sectioning

Alveolospheres were fixed with 4% paraformaldehyde (PFA) at 4°C for 2h or at room temperature for 1h, respectively. Submersion cultures of alveolospheres were first immersed in 1% low melting agarose (Sigma) and fixed with 4% PFA at room temperature for 30 min. For OCT frozen blocks, alveolospheres were washed with PBS, embedded in OCT and cryosectioned (8-10μm). For paraffin blocks, samples were dehydrated, embedded in paraffin and sectioned at 7μm.

Immunostaining on COVID-19 lungs

Immunohistochemical staining was performed on COVID-19 autopsy lung sections according to a protocol as previously described (Hou et al., 2020). Briefly, paraffin-embedded sections were baked at 60 °C for 2–4 hours and deparaffinized with xylene (2 changes × 5 min) and graded ethanol (100% 2 × 5 min, 95% 1 × 5 min, 70% 1 × 5 min). After rehydration, quenching of endogenous peroxidase was performed with 0.5% hydrogen peroxide in methanol for 15 min. Antigen retrieval was performed by boiling the slides in 0.1 M sodium citrate pH 6.0 (3 cycles with microwave settings: 100% power for 6.5 min, 60% for 6 min, and 60% for 6 min, refilling the Coplin jars with distilled water after each cycle). After cooling and rinsing with distilled water, slides washed in PBS, and blocked with 4% normal donkey serum, for an hour at RT. Primary antibody (NKX2-1:1:500, ABCA3: 1:1000, SARS-CoV-2 nucleocapsid:

1:500, Anti-SARS mouse antiserum: 1:4000, cleaved-CASP3: 1:200) were diluted in 4% normal donkey serum in PBST and incubated overnight at 4 °C. Mouse and rabbit gamma globulin was used as an isotype control at the same concentration as the primary antibody. Sections were washed in PBST, and secondary antibodies were applied for 1h at RT. After washing in PBST, the Vector® TrueVIEW Autofluorescence Quenching Kit (Vector laboratories) was used to reduce background staining, and glass coverslips were placed over tissue sections with the ProLong Gold Antifade Reagent with DAPI (Invitrogen).

Immunostaining on alveolospheres

Paraffin sections were first dewaxed and rehydrated before antigen retrieval. OCT section were defrosted and washed with PBS. Antigen retrieval was performed using 10mM sodium citrate buffer in either an antigen retrieval system (Electron Microscopy Science) or water bath (90°C for 15 min), or 0.05% Trypsin (Sigma-Aldrich) treatment for 5 min at room temperature. Sections were washed with PBS, permeabilized in PBST (0.1% Triton X-100 in PBS), and incubated with 1% BSA and 0.1% Triton X-100 in PBS for 30 min at room temperature followed by primary antibodies at 4°C overnight. Sections were then washed 3 times in PBST, incubated with secondary antibodies in blocking buffer for 1h at room temperature, washed with PBST 3 times, and mounted using Fluor G reagent with DAPI. Primary antibodies were as follows: Prosurfactant protein C (1:500), RAGE/AGER (Rat, 1:500), human RAGE/AGER (Gt, 1:500), DC-Lamp (1:250), SFTPB (Rb, 1:500), SFTPB (Ms, 1:500), ACE2 (Rb, 1:500), ACE2 (Ms, 1:500), TMPRSS2 (Rb, 1:500), TMPRSS2 (Ms, 1:250), SARS (Rb, 1:500), SARS (Ms, 1:500), Active Caspase-3 (1:500), NKX2-1(1:500), SCGB1A1 (1:250), TP63 (1:500), HTII-280 (1:250), Ki67 (1:250), ABCA3 (1:250), EPCAM (1:500), ZO1 (1:250), SOX2 (1:500).

For quantifying the stainings on near single cell suspensions, Alveolosphere bubbles were dissociated using TrypLE Select Enzyme at 37°C for 15min. Matrigel was disrupted by vigorous pipetting. Alveolosphere derived cells were then plated on matrigel precoated (5%–10% Matrigel for 30min) coverslips or chamber slides for 2-3h. Cells were then fixed in 4% paraformaldehyde.

RNA *in situ* hybridization

RNA-ISH was performed on paraffin-embedded 5 μm tissue sections of COVID-19 autopsy lungs according to the manufacturer's instructions (Advanced Cell Diagnostics). Sections were deparaffinized with xylene (2 changes × 5 min) and 100% ethanol (2 changes × 1 min), and then incubated with hydrogen peroxide for 10 min, followed by target retrieval in boiling water for 15 min, and incubation with Protease Plus (Advanced Cell Diagnostics) for 15 min at 40°C. Slides were hybridized with custom probes at 40°C for 2 hours, and signals were amplified according to the manufacturer's instructions.

Image acquisition, processing and quantification

For Alveolosphere number and size quantitation images were obtained at 1.25x objective, all other phase contrast images were taken at 10x or 20x objective using Zeiss Axiovert 200 microscope. Alveolosphere numbers and sizes were quantified using FIJI ImageJ software. Human Alveolosphere numbers and sizes (> 300 μm in perimeter) were counted on day 15, except where stated otherwise. Microscope. Scale bar 1 mm, except where stated otherwise. Confocal images were collected using Olympus Confocal Microscope FV3000 using a 20X or 40X or 60x objective.

Electron microscopy

Sample preparation for electron microscopy was performed as described previously (Jacob et al., 2017). Alveolospheres were fixed for 3h in 2.5% glutaraldehyde in 0.1M cacodylate buffer pH 7.4 at room temperature. The sample was then washed in 0.1M cacodylate buffer three times for 10min each, post-fixed in 1% Tannic Acid in 0.1M cacodylate buffer for 5min at room temperature and washed again three times in 0.1M cacodylate buffer. Alveolospheres were post-fixed overnight in 1% osmium tetroxide in 0.1M cacodylate buffer in the dark at 4°C. Samples were washed three times in 0.1N acetate buffer for 10 min and block stained in 1% Uranyl acetate for 1h at room temperature. Next, the sample was dehydrated through acetone on ice: 70%, 80%, 90%, 100% for 10min each, and then incubated with propylene oxide at room temperature for 15min. The sample was changed into EMbed 812 for 3h at room temperature followed by fresh Embed 812 and left overnight at room temperature, after which it was embedded in freshly prepared EMbed 812 and polymerized overnight at 60°C. Sections were prepared at 70 nm and grids were stained in 1% aqueous Uranyl Acetate for 5 min at room temperature followed by lead citrate for 2.5min at room temperature. Sections on grids were imaged on FEI Tecnai G^2 Twin at a magnification of 2200x and 14500x.

RNA isolation and qRT-PCR

For RNA isolation, Alveolospheres were dissociated into single-cell suspension using TrypLE Select Enzyme at 37°C for 10min. The cell pellet was resuspended in 300μl of TRIzol LS Reagent Total RNA was extracted using the Direct-zol RNA MicroPrep kit according to the manufacturer's instructions with DNase I treatment. Reverse transcription was performed using SuperScript III with random hexamer or negative-strand specific RT primer. 600ng of purified total RNA was used from each sample. The specificity of negative strand RT primer was confirmed by using viral genomic RNA purified from viral supernatants as this contains only positive strand. Negative strand RNA was detected at high levels in our infected organoids (Ct value for primer- 1202-1363, 24.76 ± 0.73; primer-848-981, 24.79 ± 0.80) compared to RNA isolated from viral inoculum (Ct value > 29). Quantitative RT-PCR assays were performed using StepOnePlus system (Applied Biosystems) with PowerUp SYBR Green Master Mix. The relative quantities of mRNA for all target genes were determined using the standard curve method. Target-gene transcripts in each sample were normalized to Glyceraldehyde 3-phosphate dehydrogenase (GAPDH). Primers used are listed in Table S3.

Bulk RNA sequencing and differential gene expression analysis

Purified RNA (1 μg) from each sample was enriched for Poly-A RNA using NEBNext Poly(A) mRNA Magnetic Isolation Module (New England BioLabs, #E7490). Libraries were prepared using NEBNext Ultra II RNA Library Prep Kit for Illumina (New England BioLabs, #E7770). Paired-end sequencing (150 bp for each read) was performed using HiSeq X with at least 15 million reads for each sample. Quality of sequenced reads were assessed using FastQC (https://www.bioinformatics.babraham.ac.uk/projects/fastqc/). PolyA/T tails were trimmed using Cutadapt (Martin, 2011). Adaptor sequences were trimmed and reads shorter than 24 bp were trimmed using Trimmomatic (Bolger et al., 2014). Reads were mapped to the reference genomes of human (hg38) and SARS-CoV-2 (wuhCor1) obtained from UCSC using Hisat2 (Kim et al., 2019) with default setting. Duplicate reads were removed using SAMtools (Li et al., 2009). Fragment numbers were counted using the featureCounts option of SUBREAD (Liao et al., 2014). Normalization and extraction of differentially expressed genes (DEGs) between control and treatments were performed using an R package, DESeq2 (Love et al., 2014).

Droplet-based single-cell RNA sequencing (Drop-seq)

Alveolospheres embedded in Matrigel were incubated with Accutase at 37°C for 20min followed by incubation with 0.25% trypsin-EDTA at 37°C for 10min. Trypsin was inactivated using DMEM/F-12 Ham supplemented with 10% FBS and cells were then resuspended in PBS supplemented with 0.01% BSA. After filtration through 40μm strainer cells at a concentration of 100 cells/μl were run through microfluidic channels at 3,000 μl/h, together with mRNA capture beads at 3,000 μl/h and droplet-generation oil at 13,000 μl/h. DNA polymerase for pre-amplification step (1 cycle of 95°C for 3 min, 15-17 cycles of 98°C for 15 s, 65°C for 30 s, 68°C for 4 min and 1 cycle of 72°C for 10 min) was replaced by Terra PCR Direct Polymerase. The remaining steps were performed as described in the original Drop-seq protocol (Macosko et al., 2015). Libraries were sequenced (150-bp paired end) using HiSeq X.

Computational analysis for Drop-seq

The FASTQ files were processed using dropSeqPipe v0.3 (https://hoohm.github.io/dropSeqPipe) and mapped on the GRCm38 genome with annotation version 91. Unique molecular identifier (UMI) counts were then further analyzed using an R package Seurat v3.0.6 (Stuart et al., 2019). UMI counts were normalized using SCTransform v0.2 (Hafemeister and Satija, 2019). Principle components which are significant based on Jackstraw plots were used for generating t-SNE plots. After excluding duplets, specific cell clusters were identified based on enrichment for *Sftpc*, *Sftpa1*, *Sftpa2*, *Sftpb*, *Lamp3*, *Abca3*, *Hopx*, *Ager*, *Akap5*, *Epcam*, *Vim*, *Pdgfra*, *Ptprc*, *Pecam1* and *Mki67* in tSNE plot.

Computational analysis for single-cell RNA sequencing of COVID-19 patient lungs

Publicly available single-cell RNA-seq dataset of six severe COVID-19 patient lungs (GEO: GSE145926; Bost et al., 2020) and control lungs (GEO: GSE135893; Habermann et al., 2019) were obtained from Gene Expression Omnibus (GEO). *EpCAM*-positive epithelial cell cluster in the severe COVID-19 patient lungs was further clustered based on *LAMP3*, *ABCA3*, *KRT5*, *KRT15*, *DNAH1*, *FOXJ1*, *SCGB3A1* and *SCGB1A1*. AT2s that have ≧ 1 UMI count of LAMP3, NKX2-1 and ABCA3 were utilized for comparison between severe COVID-19 patient lungs and control lungs. UMI counts were normalized and regressed to percentage of mitochondrial genes using SCTransform. Enriched genes in severe COVID-19 patient and control lungs were extracted using FindMarkers and shown in volcano plot drawn by R package Enhanced Volcano v1.5.4 Genes that have ≧ 2 log2 fold change were used as input for Enrichr (Kuleshov et al., 2016) query to get enriched signaling pathways through database - BioPlanet.

QUANTIFICATION AND STATISTICAL ANALYSIS

Statistical methods relevant to each figure are outlined in the figure legend. Sample size was not predetermined. Data are presented as means with standard error (SEM) to indicate the variation within each experiment. Statistics analysis was performed in Excel, Prism and R. A two-tailed Student's t test was used for the comparison between two experimental conditions. For experiments with more than two conditions, statistical significance was calculated by ANOVA followed by the Tukey-HSD, Steel-Dwass or Dunnett's test for multiple comparisons. We used Shapiro-Wilk test to test whether data are normally distributed and used Wilcoxon rank sum test for the comparison between two conditions that showed non-normal distributions.